

# Observing Earthquakes Triggered in the Near Field by Dynamic Deformations

by Joan Gomberg, Paul Bodin, and Paul A. Reasenber

**Abstract** We examine the hypothesis that dynamic deformations associated with seismic waves trigger earthquakes in many tectonic environments. Our analysis focuses on seismicity at close range (within the aftershock zone), complementing published studies of long-range triggering. Our results suggest that dynamic triggering is not confined to remote distances or to geothermal and volcanic regions. Long unilaterally propagating ruptures may focus radiated dynamic deformations in the propagation direction. Therefore, we expect seismicity triggered dynamically by a directive rupture to occur asymmetrically, with a majority of triggered earthquakes in the direction of rupture propagation. Bilaterally propagating ruptures also may be directive, and we propose simple criteria for assessing their directivity. We compare the inferred rupture direction and observed seismicity rate change following 15 earthquakes ( $M$  5.7 to  $M$  8.1) that occurred in California and Idaho in the United States, the Gulf of Aqaba, Syria, Guatemala, China, New Guinea, Turkey, Japan, Mexico, and Antarctica. Nine of these mainshocks had clearly directive, unilateral ruptures. Of these nine, seven apparently induced an asymmetric increase in seismicity rate that correlates with the rupture direction. The two exceptions include an earthquake preceded by a comparable-magnitude event on a conjugate fault and another for which data limitations prohibited conclusive results. Similar (but weaker) correlations were found for the bilaterally rupturing earthquakes we studied. Although the static stress change also may trigger seismicity, it and the seismicity it triggers are expected to be similarly asymmetric only if the final slip is skewed toward the rupture terminus. For several of the directive earthquakes, we suggest that the seismicity rate change correlates better with the dynamic stress field than the static stress change.

## Introduction

We explore the hypothesis that transient dynamic deformations associated with seismic waves can trigger earthquakes in a range of tectonic environments and at short distances from the triggering earthquakes. Dynamic triggering has been accepted as a likely process at remote distances (greater than several rupture lengths) and/or within geothermal regions (Hill *et al.*, 1993, 1995; Protti *et al.*, 1995; Gomberg and Davis, 1996; Singh *et al.*, 1998; Brodsky *et al.*, 2000; Mohamad *et al.*, 2000; Gomberg *et al.*, 2001; Hough, 2001; Power *et al.*, 2001), while static stress changes are usually invoked to explain aftershocks. It is possible that dynamic triggering occurs at closer distances as well (i.e., in aftershock zones), together with static stress triggering, and not only in geothermal areas. If so, this would have implications for how earthquakes interact and begin to rupture.

If this hypothesis is true, increases in the regional seismicity shortly after a mainshock will tend to correlate with the pattern of radiated seismic energy. In particular, if the

rupture in the mainshock is asymmetric (e.g., when rupture is unilateral), the pattern of seismicity rate increase will tend to be asymmetric as well. In contrast, the static stress change produced by the same mainshock, which depends only on the final slip distribution (and not on the dynamics of the rupture), will tend to produce a different pattern of seismicity increase. The contrast in the expected patterns of triggered events can help in assessing the relative roles played by static and dynamic stresses.

It is well known that the dynamic deformations that radiate in the direction of the rupture propagation are larger than those that radiate in the opposite direction (see, e.g., Somerville *et al.*, 1997). Figure 1 illustrates the radiation asymmetry for a simple Haskell model of a unilaterally propagating rupture (Haskell, 1964; Aki and Richards, 1980). The pattern of seismicity rate increase in this model is asymmetric, being more pronounced in the direction of rupture propagation. In a Haskell model of a unilateral rupture, the destructive (and constructive) interference in the back (and

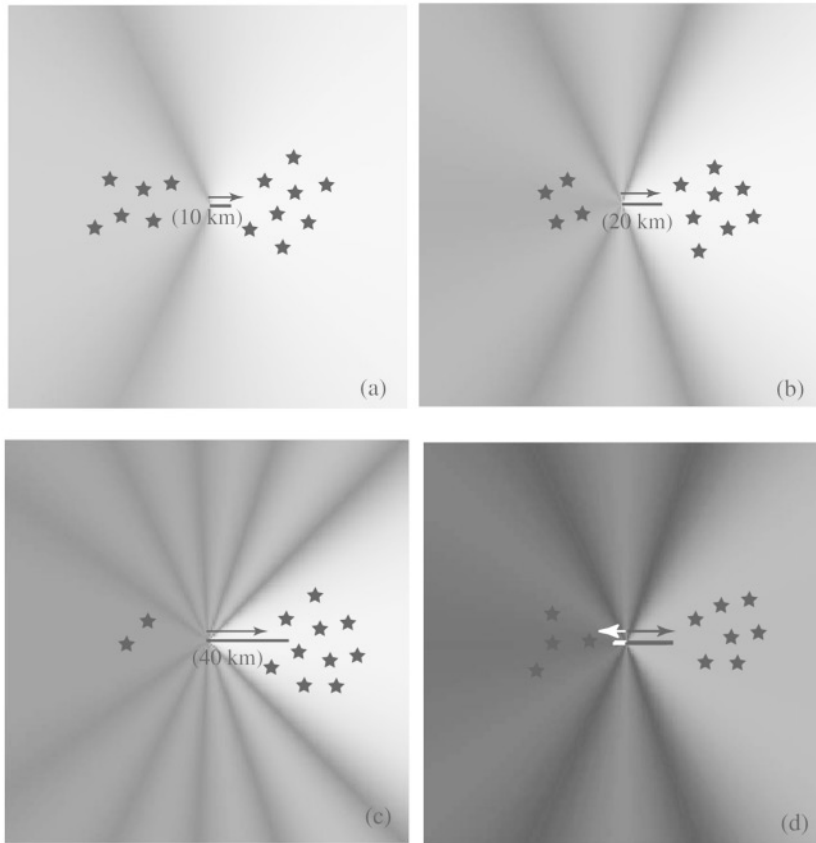


Figure 1. The spatial pattern of the seismic-wave spectral amplitude at 5 sec period calculated for a far-field Haskell model of the unilateral rupture (Aki and Richards, 1980). Shading shows relative amplitude variations, with lighter shading indicating larger amplitudes. The fault locations and rupture directions are indicated by the horizontal lines and arrows, respectively. As the rupture length (listed under each fault) grows (a–c) the focusing of radiated seismic waves becomes more pronounced in the direction of rupture propagation (becomes “directive”). Our hypothesis is illustrated by the stars, which denote epicenters of aftershocks triggered by the directive rupture on the larger fault. As the focusing becomes stronger, if aftershocks are dynamically triggered they should be relatively more abundant in the direction of focusing. Panel (d) shows that a bilateral rupture may be considered as the superposition of two unilateral ruptures and will be directive toward the end of the longer fault segment as long as half or more of the moment is released along that segment. The dynamically triggered seismicity will be asymmetric with a greater rate increase in the directive direction.

forward) direction strengthens as the rupture length grows. Actual earthquakes, whose ruptures are more complex, can be represented as a sum of unilateral models with varying direction. Thus, a bilateral rupture (one consisting of two rupture segments separated by the epicenter) can also produce a directional radiation field if the maximum moment release occurs on the longer segment. In this case, the maximum wave amplitudes would be focused in the direction of propagation along this segment (Fig. 1).

A number of published studies show that observed focusing of seismic waves is generally consistent with the model of directivity described above. Boore and Joyner (1978) showed through analytical and statistical modeling that a relative focusing of radiated energy in the rupture propagation direction still is apparent for a large range of variability in rupture velocity and slip. Somerville *et al.* (1997) documented azimuthally dependent amplitude and duration variations consistent with directivity effects. Their empirical study employed recordings of earthquakes of magnitude 6.0 and larger at distances up to 50 km. They suggested that directivity effects should be insignificant for magnitude 6.0 and smaller earthquakes and at distances beyond 50 km, where path effects dominate. However, most recently, Miyake *et al.* (2001) showed that directivity effects are observable for earthquakes ranging from  $M_{\text{JMA}} 4.9$  to  $M_{\text{JMA}} 7.2$  ( $M_{\text{JMA}}$  is Japanese Meteorological Agency [JMA] magnitude) at near-source to 50-km distances. They found

an azimuthal dependence of source spectra consistent with directivity effects predicted theoretically and noted that this dependence did not differ significantly for strike-slip or dip-slip mainshocks.

As just described, simple predictions about the spatial distribution of dynamically triggered seismicity can be made based on our understanding of rupture directivity, thereby providing a simple observational test of the plausibility of dynamic triggering. We emphasize that we are not testing the viability of a particular model of dynamic triggering, but are only making an observational test of its plausibility. We are unable to think of a comparable test that employs observations of the timing of triggered seismicity, particularly since most physical failure models cannot explain the finite durations of dynamically triggered earthquake sequences (Gomberg, 2001). However, we suggest that the failure to find a physical model to explain an observation does not mean the observation should be discounted, but simply that our understanding of the underlying process is incomplete. Although our study focuses on spatial patterns, we comment on some of the interesting temporal observations as motivations for additional studies.

In this article, we first present our interpretation of several published studies whose observations and conclusions directly shed light on our hypothesis. We then describe our own analysis of seismicity rate change and rupture directivity associated with 13 earthquakes (Table 1). In bringing

Table 1  
Source Parameters

Earthquake (Ref.)	Magnitude	Date (mm/dd/yy)	Origin Time	Hypocenter Latitude	Hypocenter Longitude	Rupture Segment Lengths	Rupture Type, Propagation Direction
Coyote Lake (Bouchon, 1982)	$M_s$ 5.7	08/06/79	17:05:22.9	37.1042° N	121.513° W	12 km S, 2 km N	Directive south
Superstition Hills (Wald <i>et al.</i> , 1990)	$M_w$ 6.6	11/24/87	13:15:56.7	33.0145° N	115.852° W	18 km S, 2 km N	Directive, southeast
Gulf of Aqaba (Klinger <i>et al.</i> , 1999)	$M_w$ 7.3	11/22/95	04:15:11.9	28.83° N	34.79° W	~70 km N	Directive, north
Guatemala (Young <i>et al.</i> , 1989)	$M_s$ 7.5	02/04/76	09:01:43.9	15.30° N	89.1° W	210 km W, 60 km E	Directive, west
Kokokili (van der Woerd <i>et al.</i> , 2002)	$M_w$ 7.8	11/14/01	09:26:10.3	36.01° N	90.50° E	~300 km E	Directive, east
Papua New Guinea (Yagi and Kikuchi, 2000a)	$M_w$ 8.1	11/16/00	04:54:56.7	3.97° S	152.32° E	185 km S, 15 km N	Directive, south
Hector Mine (Ji <i>et al.</i> , 2002)	$M_w$ 7.1	10/16/99	09:46:41.1	34.597° N	116.27° W	37 km S, 17 km N	Directive, south
Izmit (De Louis <i>et al.</i> , 2000)	$M_w$ 7.4	08/17/99	0:01:37.60	40.76° N	29.97° E	90 km E, 55 km W	Directive, east
Tottori (Yagi and Kikuchi, 2000b)	$M_w$ 6.6	10/06/99	13:30:18.0	35.275° N	133.350° E	10 km N, 10 km S	Maybe directive, southeast
Kobe (Wald, 1996)	$M_w$ 6.9	01/16/95	20:46:52.1	34.58° N	135.02° E	40 km E, 20 km W	Not directive
Tehuacan (Singh <i>et al.</i> , 1999)	$M_w$ 7.0	06/15/99	20:42:0.7	18.15° N	97.52° W	53 km total	Directive, northwest
Borah Peak (Mendoza and Hartzell, 1988)	$M_w$ 7.3	10/28/83	14:06:06.6	44.08° N	113.857° W	44 km N, 8 km S	Directive, north
Oaxaca (Hernandez <i>et al.</i> , 2001)	$M_w$ 7.5	09/30/99	1:63:11.5	16.00° N	97.02° W	67.5 km N, 22.5 km S	Directive, northwest

Magnitudes, hypocenters, origin times, and rupture segment lengths and directions for the 13 earthquakes we studied.  $M_w$  and  $M_s$  are moment and surface-wave magnitudes, respectively.

together these diverse cases, we attempt to apply a uniform method and standard for detecting correlations between patterns of triggered seismicity and the direction of rupture propagation in the respective mainshocks. Our study is an exploratory one and is not designed to quantitatively or definitively test the hypothesis, or to rule out the possibility of other mechanisms for earthquake triggering, including those involving static stress changes.

### Published Studies

Here we summarize the results of published studies of four earthquakes that putatively triggered seismicity at remote or near-field distances. In this context “remote” refers to distances exceeding several rupture dimensions and “near field” to lesser distances, the latter also often referred to as the aftershock zone. We begin with the  $M_w$  7.3, 1995 Gulf of Aqaba earthquake for which Mohamad *et al.* (2000) documented an increased seismicity rate approximately 500 km to the north along the Dead Sea fault system. Klinger *et al.* (1999) infer a northward-propagating rupture for this event by modeling its teleseismic broadband body waves. While their observations are consistent with our hypothesis, other observations complicate the picture. The seismic waves that provide evidence of directivity and the seismicity were observed at differing distances. We also cannot rule out the possibility that remotely triggered seismicity also occurred to the south of the mainshock, but was not documented. It is interesting to note that the rate increase (from about 0.5–1.0 events/day to 21 events/3.5 hr) appears to be delayed according to the criteria in Hill *et al.* (1993), with the first triggered event occurring 167 min after the mainshock. Standard dynamic or static triggering models do not explain this

delayed rate change (i.e., they may explain delayed failure of an individual fault, but not delayed rate change). Unlike many other examples of remotely triggered seismicity, the seismicity increase is at least 50 km from known volcanic or geothermal areas.

Both remote and near-field triggering by the  $M_w$  7.3, 1992 Landers, California, earthquake are consistent with our hypothesis. The Landers earthquake rupture propagated almost purely unilaterally to the north-northwest (Wald and Heaton, 1994), and the most significant increases in seismicity rate occurred north-northwest of the rupture at all distances (Hill *et al.*, 1993; Kilb *et al.*, 2000). Both Gomberg (1996) and Kilb *et al.* (2000) explicitly compared the dynamic deformation changes and seismicity rate changes. In both studies, directive radiation was documented by surface recordings of the dynamic displacement field at the same distances as the seismicity. The results of both studies were consistent with the hypothesis that a rupture propagating to the north-northwest should trigger seismicity in the same direction. However, Gomberg (1996) found that if triggered seismicity was explained in terms of a Coulomb failure criterion, then the correlation was unclear because no triggered rate changes were observed where the dynamic Coulomb stresses were maximum. On the other hand, in the near field, Kilb *et al.* (2000) found a strong correlation between the pattern of dynamic Coulomb stresses and seismicity rate changes. They also found the correlation between rate change and dynamic Coulomb stress changes more compelling than that between the rate change and static Coulomb stress changes.

The  $M_w$  7.1, 1999 Hector Mine, California, earthquake occurred 20 km from the Landers earthquake. Its rupture appears to have been directive toward the south, according

to our criterion, although its complexity makes this determination uncertain (Dreger and Kaverina, 2000; Ji *et al.*, 2002). The Hector Mine earthquake triggered remote seismicity to the south in three clusters and to the north at Long Valley (Gomberg *et al.*, 2001). Two of the three clusters to the south and the Long Valley cluster occurred in volcanic or geothermal areas. However, the site of the third southern cluster, at Indio, California, is neither volcanic nor geothermal. We investigate the pattern of near-field seismicity rate changes associated with the Hector Mine earthquake in a following section.

The  $M_w$  8.1, 1998 Antarctic earthquake sequence is well suited for stress transfer studies (Toda and Stein, 2000). The sequence occurred far from any plate boundary in a region that had been essentially aseismic. Toda and Stein (2000) found that 60%–94% of the aftershocks occur in regions of increased static Coulomb failure stress (85%–93% if the rupture is shifted 18–25 km eastward, which is within the range of published rupture models). Toda and Stein (2000) also note, however, that these correlations require very specific model assumptions. According to our simple criteria for a directive rupture, all the rupture models considered by Toda and Stein (2000) are strongly directive to the west (see their Figure 2). For all except one of their rupture models, there is at most one aftershock off the eastern end of the rupture and three or more off the western end (see their Figure 3). For the exceptional model, the rupture fills the entire east-west extent of the aftershock zone and occurs as two sub-events. This exception would be consistent with our hypothesis if the second subevent were considered as a separate event. Indeed, Henry *et al.* (2000) and Nettles *et al.* (1999) modeled the mainshock as a westward-propagating rupture up to approximately 140 km in length, followed by a second event starting approximately 40 sec later and nearly 100 km from the termination of the first event. Finally, the occurrence of aftershocks extending 80 km to the south of the Antarctic mainshock does not violate our hypothesis, which pertains only to asymmetries in seismicity rate changes at the ends of a propagating rupture. Whether these aftershocks to the south are better explained by static or dynamic stress transfer or some other mechanism is beyond the scope of this study.

## Analysis of Seismicity for Directive and Nondirective Earthquakes

### Measuring Seismicity Rate Change

Because of inherent limitations of earthquake catalogs and the variability of aftershock patterns from case to case, we must make some subjective choices in characterizing the seismicity rate changes associated with each mainshock. We characterize the seismicity rate changes associated with a triggering mainshock using the  $\beta$ -statistic derived by Matthews and Reasenberg (1988) (see the Appendix for details). The idea underlying the  $\beta$ -statistic is that it provides a mea-

sure of the significance of a rate change and represents the difference between the number of earthquakes observed following the mainshock in some after time period,  $t_a$ , and the number expected if earthquake occurrence were to continue at the rate before the mainshock. The latter is measured for some “background” period,  $t_b$ , before the mainshock. The significance of this difference between the observed and expected number of earthquakes is estimated by normalizing it by an estimate of the variance of the background rate. Noting that there are various approaches to estimating the  $\beta$ -statistic that differ in their underlying statistical assumptions (e.g., Kilb *et al.*, [2000] use a slightly different form) and that the validity of these assumptions often cannot be verified, we only interpret the relative spatial variation in the  $\beta$ -statistic within a single region without defining some absolute significance level. The  $\beta$ -statistic is computed on a 1-km grid for the seismicity within 5-km-radius circular areas centered on each grid point, thus producing a smoothed “ $\beta$ -map” (for example, see Fig. 2a). Unless otherwise specified, we chose  $t_a = 60$  days, yielding a conservative estimate of  $\beta$  because the most significant rate increase generally occurs within a period much shorter than 60 days. We verify the immediacy of significant rate increases by examining time histories of the seismicity.

We used the most complete and accurate seismicity catalog available for each earthquake studied. We assume that all earthquakes are independent except for a possible dependence on the triggering mainshock being studied. Thus, we select background and after periods so that the catalog used contains only earthquakes below some maximum magnitude. We excluded earthquakes with magnitudes smaller than the minimum magnitude,  $M_{\min}$ , above which detection is believed to be complete. Further, we tried to ensure that apparent asymmetries in rate changes were not produced by changes in detection related to incomplete processing or enhanced recording and attention following the mainshock. We divide each catalog into four subsets, corresponding to the background and after periods and to the two areas surrounding the mainshock divided by a line perpendicularly bisecting the mainshock rupture length. For each subset we estimate  $M_{\min}$  as the magnitude below which the observations deviate from a Gutenberg-Richter relation. The regions selected for completeness analyses are often larger/longer than those used to compute the rate change maps shown below because we examined the larger area to look for more remote rate increases, which were not observed. A larger area also was often necessary to have a sufficiently large sample to define a Gutenberg-Richter relation. We conservatively adopt the largest value of  $M_{\min}$  for use in the seismicity rate analysis for that earthquake. We report catalog magnitudes without reference to their type because the absolute numbers are relatively unimportant as long as the magnitude measurement is consistent throughout the catalog. Table 2 lists the catalog characteristics corresponding to each of the earthquakes we studied.

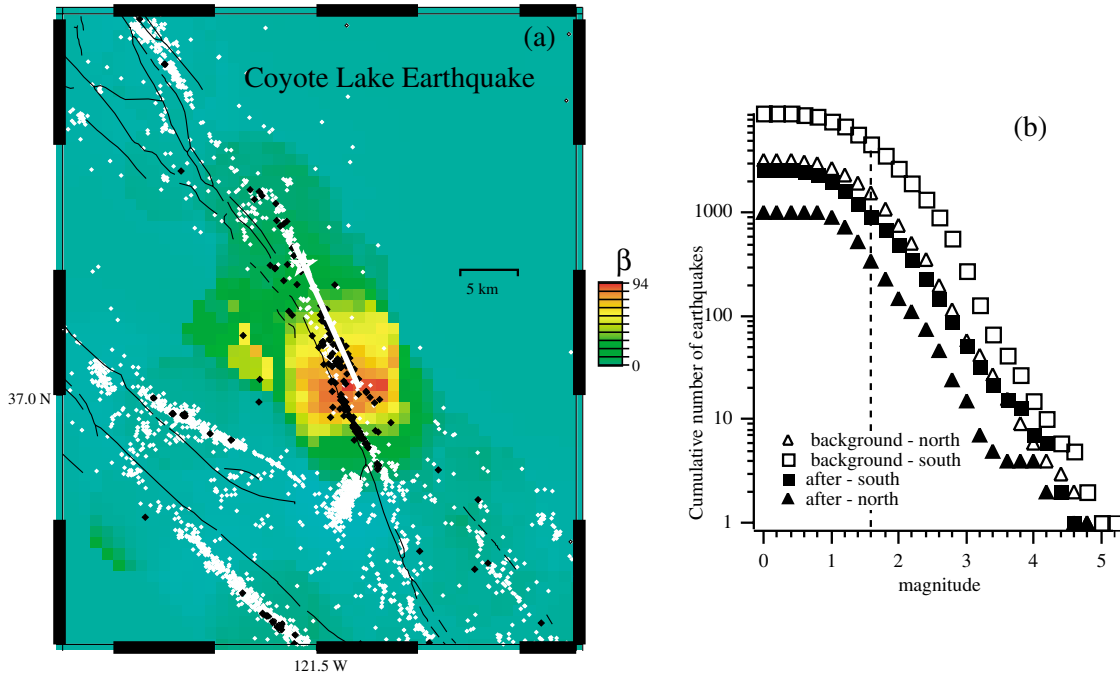


Figure 2. (a) Map of seismicity and  $\beta$ -statistic calculated for the Coyote Lake earthquake. White and black symbols indicate epicenters of earthquakes in the background and after periods, respectively, that were used to calculate  $\beta$  (equation 1 in Appendix).  $\beta$  indicates change in average seismicity rate in after period relative to background period, with red color indicating maximum rate increase; no rate decreases were observed. The white star shows the mainshock epicenter. The white line is the projection of the (nearly vertical) rupture plane on the surface. Thin black lines show mapped faults and geographic features. (b) Cumulative number of cataloged earthquakes studied in the selected time period and geographic region surrounding the Coyote Lake earthquake (see Table 2). It is assumed that the earthquakes follow a Gutenberg-Richter distribution above the magnitude  $M_{\min}$ , which is graphically estimated (dashed vertical line). Because  $M_{\min}$  may vary spatially and temporally, we divide the catalog into the four subsets shown and use the largest estimate of  $M_{\min}$  as a lower cutoff for our rate analysis. (Results were not sensitive to variations of  $M_{\min}$  of several tenths of a magnitude unit.)

### Correlating Rupture Directivity with Seismicity: Case Studies

We now examine the correlation between the observed seismicity rate changes and the inferred or measured dynamic deformations for a suite of 13 triggering earthquakes (Table 1). We expect the greatest correlation for strike-slip events because the rupture propagation direction corresponds to maxima in the shear-wave radiation pattern and because our intuition suggests that shear waves, the largest amplitude waves, would be most likely give rise to dynamic triggering. We begin with six strike-slip events that are unambiguously directive, having either unilateral ruptures or asymmetrical bilateral ruptures, and three strike-slip events for which rupture directivity is unclear. We consider a rupture to be unilateral if at least 80% of its length is on one side of the hypocenter. We also look at three normal-faulting events with horizontally directive ruptures. (For these, the propagation direction is nodal for shear-wave radiation.)

This selection of earthquakes is not exhaustive, and some well-observed earthquakes have been omitted. For example, the 1989  $M_w$  7.0 Loma Prieta earthquake was omitted because of significant uncertainties concerning which faults actually ruptured and the distribution of aftershocks (McLaughlin *et al.*, 1999). The latter apparently results from a strong dependence on the complex seismic velocity structure, which may actually control aftershock generation and also introduces error in estimated locations (Eberhart-Phillips and Michael, 1998). Although clearly bilateral (see Wald *et al.* [1991] for a comparison of rupture models), uncertainties regarding the rupture planes and slip render our criteria for assessing directivity inapplicable.

*M<sub>s</sub> 5.7 Coyote Lake, California.* An asymmetry in the dynamic deformation field of this strike-slip earthquake is observed directly and within the same distance range as the seismicity. A unilateral north-to-south-propagating rupture is constrained by modeling of regional waveform data, albeit

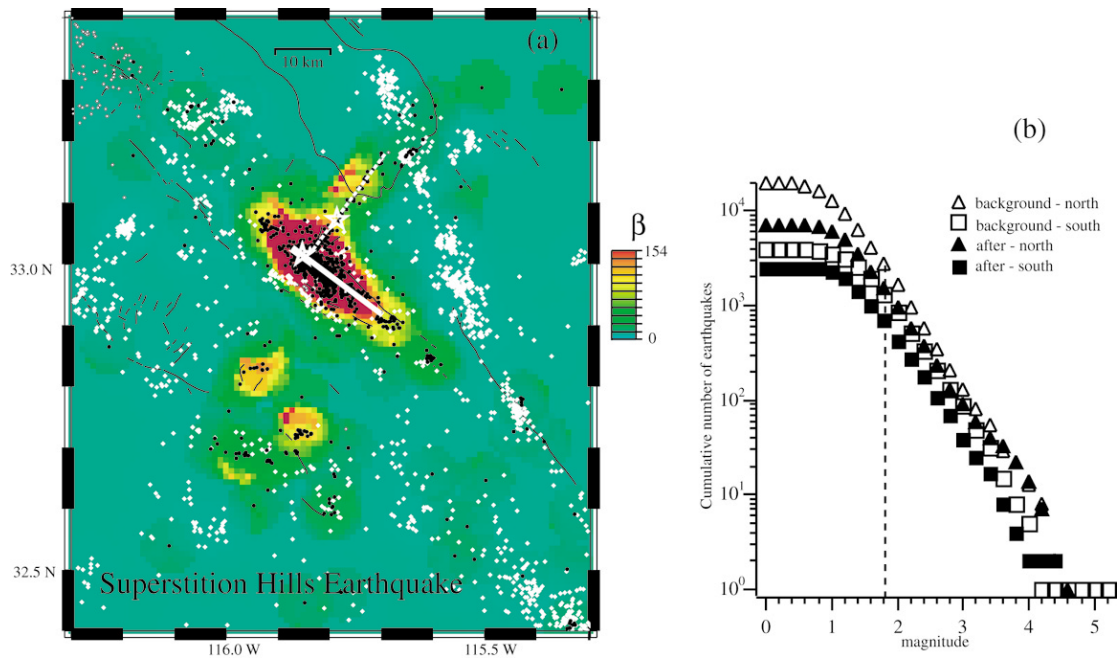


Figure 3. (a) Map of seismicity and  $\beta$ -statistic calculated for the Superstition Hills earthquake. The dashed line and stars show locations of the Elmore Ranch rupture and epicenter, respectively. (b) Cumulative number of cataloged earthquakes in the time period and geographic region surrounding the Superstition Hills (see Table 2). See Figure 2 caption for further details.

Table 2  
Catalog Analysis Parameters

Earthquake	Catalog	Min. Mag. of Cmp.	Background Period		After Period		Geographic Boundaries	
			Start Date (mm/dd/yy)	End Date (mm/dd/yy)	Start Date (mm/dd/yy)	End Date (mm/dd/yy)	Longitude	Latitude
Coyote Lake	CNSS	1.6	8/6/69	8/6/79	8/6/79	8/5/81	120.5° to 122.5° W	36.1° to 38.1° N
Superstition Hills	CNSS	1.8	1/1/82	11/24/87	11/24/87	11/24/89	114.9° to 116.9° W	32.0° to 34.0° N
Gulf of Aqaba	ISC	3.0	1/1/92	11/22/95	11/22/95	12/31/96	33.3° to 36.3° E	27.3° to 30.3° N
Gulf of Aqaba	NEIC (PDE)	4.3	1/1/85	11/22/95	11/22/95	12/31/99	33.3° to 36.3° E	27.3° to 30.3° N
Guatemala	MIDAS-IPGH	4.0	1/1/66	2/4/76	2/4/76	12/31/77	86.75° to 92.75° W	12.0° to 18° N
Kokoxili	NEIC (PDE)	4.5	1/14/90	11/14/01	11/14/01	1/14/02	88.5° to 96.5° E	33.5° to 38.0° N
Papua New Guinea	NEIC (PDE)	4.5	1/5/95	11/15/00	11/16/00	5/4/01	149.0° to 155.0° E	1.0° to 6.0° S
Hector Mine	CNSS	2.0	9/1/86	12/31/91	10/16/99	6/30/00	115.3° to 117.3° W	33.6° to 35.6° N
Izmit	Kandilli Observ.	2.8	1/1/98	8/17/99	8/17/99	11/12/99	28.0° to 32.0° E	38.76° to 42.76° N
Tottori	JMA	2.5	9/8/91	10/6/00	10/6/00	4/10/01	132.75° to 134.75° E	34.28° to 36.28° N
Kobe	JMA	2.6	1/1/85	1/16/95	1/16/95	9/30/97	133.52° to 136.52° E	33.08° to 36.08° N
Tehuacan	SSNM	3.9	1/1/98	6/15/99	6/15/99	12/31/99	95.52° to 99.52° W	16.15° to 20.15° N
Borah Peak	CNSS	3.0	12/1/73	10/28/83	10/28/83	10/27/85	115.85° to 111.85° W	42.0° to 46.0° N
Oaxaca	SSNM	4.0	1/1/98	9/30/99	9/30/99	12/31/99	95.0° to 99.0° W	14.0° to 18.0° N

Geographic regions and time periods used to define a Gutenberg–Richter relation and to determine the minimum magnitude of completion for the 13 earthquakes we studied. MIDAS-IPGH, Middle America Seismograph Consortium–Institute of Pan-American Geography and History; SSN, Servicio Seismologico Nacional de Mexico; JMA, Japan Meteorological Agency; NEIC (PDE), National Earthquake Information Center Preliminary Determination of Epicenters; CNSS, Council of the National Seismographic System; ISC, International Seismological Center.

sparse, which also provides constraint on the rupture geometry and length (Bouchon, 1982; Liu and Helmberger, 1983). We assume that the stress and strain fields at seismogenic depth share similar patterns as the measured surface displacement wave field.

Figure 2a reveals a clear rate increase at and beyond the

southern end of the rupture, consistent with a focusing of dynamic deformations southward due to directivity. We compute  $\beta$ -maps using  $M \geq 1.6$  earthquakes in the Council of the National Seismic System (CNSS) catalog (Fig. 2b). We note that the final slip distribution is relatively symmetric (Bouchon, 1982; Liu and Helmberger, 1983); that is, the

maximum slip is centered on the rupture and decreases radially, although there is some variability in the slip gradients at the edges of the rupture in the model of Liu and Helmburger (1983). Although this and other factors we have not considered may influence both the static and dynamic stress changes, we suggest that these are probably second-order effects (and not constrained by any observations). In contrast, the clearest, most well-resolved asymmetry in the source model is that associated with the unilateral rupture propagation, which is a feature of the rupture model required by the seismic data and affects only the pattern of dynamic deformations. This suggests that the dynamic stress changes may have a greater role in producing the asymmetric seismicity rate change pattern for this event than the static stress changes, although additional work is required to test this.

*M<sub>w</sub> 6.6 Superstition Hills, California.* Although also a nearly unilateral rupture, the Superstition Hills earthquake is a more complex case because it was preceded (by 11 hr) by the conjugate *M<sub>w</sub> 6.2 Elmore Ranch* earthquake. There is no way to separate the aftershock sequences of the two events (Fig. 3a). The Superstition Hills earthquake ruptured primarily to the southeast (see Figure 10 of Frankel and Wernberger, 1989). As with the Coyote Lake earthquake, an asymmetry in the dynamic deformation field is observed in surface seismograms recorded within the same distance range as the seismicity. Models of the Superstition Hills rupture based on teleseismic or strong-motion data consist of two or three subevents (Hwang *et al.* [1990] and Wald *et al.* [1990], respectively), with more of the moment being released by the subevents more distant from the hypocenter.

We compute  $\beta$ -maps using the CNSS catalog with  $M_{\min}$  2.8 (Fig. 3b). Contrary to our hypothesis, the seismicity rate change does not appear greater at the southern end of the Superstition Hills fault, where directivity should enhance dynamic deformations (Fig. 3a). The relative abundance of aftershocks at the northern end of the rupture includes aftershocks of the Elmore Ranch earthquake, which may mask an asymmetry in seismicity rate increase associated with the Superstition Hills rupture. Contributions from static stress triggering might also reduce any asymmetry, as the final static slip distribution inferred from geodetic data is skewed toward the northernmost 10-km stretch of the Superstition Hills fault (Larsen *et al.*, 1992).

Three small-magnitude clusters are located southwest of the Superstition Hills fault, one of which is approximately on-strike with the Elmore Ranch rupture. However, a symmetric slip distribution (Larsen *et al.*, 1992) and a bilateral rupture with the longer segment to the northeast of the hypocenter do not suggest that the Elmore Ranch event was directive to the southwest. We conclude that the Superstition Hills earthquake is inconsistent with our hypothesis. However, the complicating effects of the Elmore Ranch earthquake prevent us from concluding that this case contradicts the hypothesis.

*1995 M<sub>w</sub> 7.3 Gulf of Aqaba.* Both the geometry of faulting (location of hypocenter relative to the total rupture) and the observed wave field constrain this rupture to be a unilateral (south-to-north) and approximately vertical strike-slip rupture. This event appears to have triggered seismicity at remote distances (approximately 500 km) to the north (Mohamad *et al.*, 2000). No on-scale near-field mainshock seismograms were recorded. To our knowledge, no catalog based on local or regional network data exists for this area and time period. Thus, we used the global National Earthquake Information Center (NEIC) *Preliminary Determination of Epicenter* (PDE) and International Seismological Center (ISC) catalogs (Table 2) to characterize the seismicity rate changes associated with this event (Fig. 4).

Although the general rate pattern does not change significantly with variations in  $t_b$ ,  $t_a$ , smoothing, or catalog, we suggest that the pattern is not indicative of the true rate change. The background rate is sufficiently low that the aftershock distribution determines where the most significant rate increases occur (e.g., increasing  $t_b$  by a few years adds only a few events). We note that the aftershock or rate change pattern apparent in the ISC and PDE catalogs are rotated approximately 20° counterclockwise from the fault trace (Fig. 4a) and do not look like the pattern reported in Klinger *et al.* (1999), which should be more accurate as it is based on data from a dense network of temporary seismographs deployed in the epicentral area. Klinger *et al.* (1999) found that the greatest concentration of aftershocks occurred toward the northern end of the rupture, which is suggestive evidence of consistency with our hypothesis. However, we conservatively draw no conclusions about this event.

*1976 M<sub>s</sub> 7.5 Guatemala.* Waveform modeling of teleseismic body waves shows this earthquake to be directive, with 70% of the moment released in a westward-propagating rupture along an approximately 210-km-long fault segment west of the hypocenter (Fig. 5a). The eastward-propagating portion of the rupture released the remaining 30% of the moment, mostly along an approximately 60-km-long segment east of the hypocenter (Young *et al.*, 1989). Isoseismal maps provide additional, independent evidence of the directive nature of this rupture assuming that seismic waves cause damage and other effects characterizing intensities. The isoseismals are skewed in the direction of rupture propagation (Fig. 6). Although imprecise, a benefit of using intensity observations is that they should be independent of static stress changes.

We compute  $\beta$ -maps using the Middle America Seismograph Consortium–Institute of Pan-American Geography and History (MIDAS-IPE) catalog (Fig. 5). Although the seismicity in this area is sparse, it suggests an asymmetric distribution consistent with our hypothesis. The temporal pattern of the earthquakes in the after period suggests they were triggered: 9 of the 12 events off the southwest end of the rupture occurred within 5 days of the mainshock, and four of these within 24 hr. Among this southwestern group of

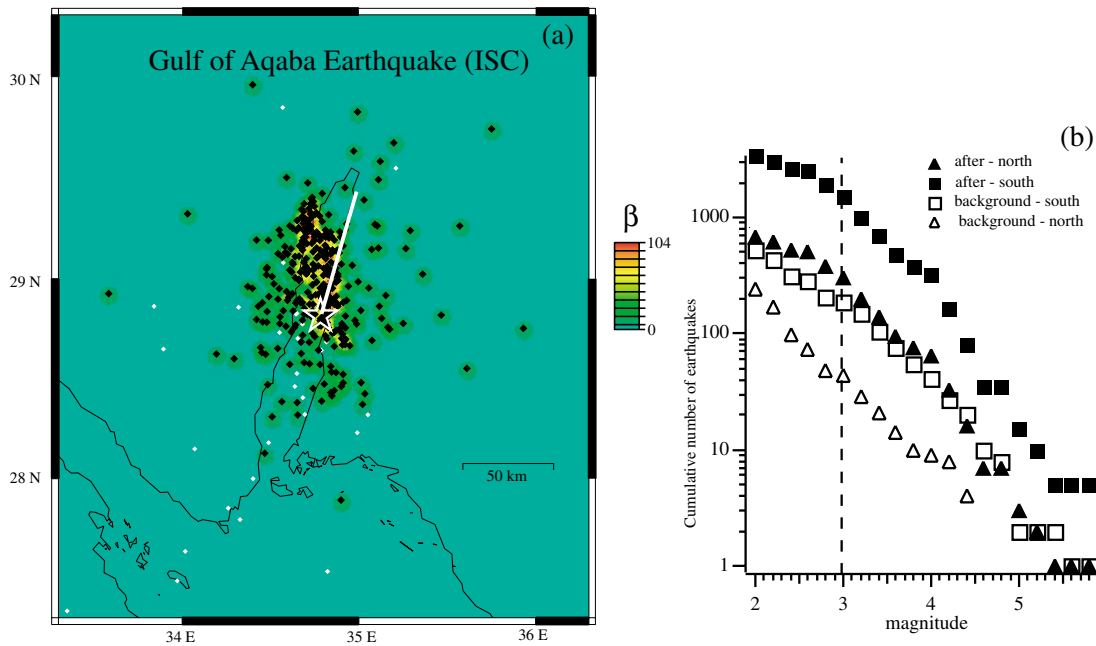


Figure 4. (a) Map of seismicity and  $\beta$ -statistic calculated with the ISC catalog for the Gulf of Aqaba earthquake. (b) Cumulative number of earthquakes cataloged by the ISC in the time period and geographic region surrounding the Gulf of Aqaba earthquake (see Table 2). Comparable figures were generated for the PDE catalog (Table 2). For unknown reasons, the PDE catalog appears to be complete above a larger magnitude  $M_{\min}$  than the ISC catalog (Table 2); both catalogs yield similar rate change patterns. For PDE and ISC rate change calculations, we start the background period in January 1994 to avoid including a vigorous earthquake swarm located just south of the epicenter in August 1993. See Figure 2 caption for further details.

earthquakes was an  $M$  5.8 earthquake, which occurred 2 days after the mainshock, so that some of these events could be secondary aftershocks (all others had  $M < 5.0$ ). In contrast, only three events occurred off the eastern end of the fault, two within the first 5 days. One of these was an  $M$  6.5 event, so the two nearby events may also be secondary aftershocks.

The contribution of static stress changes to the asymmetric aftershock distribution cannot be assessed. Surface displacements appear to increase toward the western end of the fault (Plafker, 1976), but Young *et al.* (1989) find no evidence in their waveform modeling for greater displacements at either end of the fault.

The relationship of this earthquake to the intense cluster of earthquakes just offshore and southeast of the rupture is unclear. The first event in the cluster occurred 2 days after the mainshock and was followed by a few events after 31–38 days and three more events at 89–90 days.

**2001  $M_w$  7.8 Kokoxili, China.** This earthquake ruptured the surface for nearly 300 km. Asymmetric radiation of dynamic deformations is observed in teleseismic body waves, which are used to infer a unilateral eastward-propagating rupture (Kikuchi and Yamanaka, 2001). This rupture model is consistent with a hypocenter located at the western end of the surface rupture, which probably reached nearly 300 km (van der Woerd *et al.*, 2002) and a Harvard centroid moment

tensor (CMT) centroid location (Dziewonski *et al.*, 1981; Ekström, 1994) at the rupture's center.

To our knowledge no local network and catalog exist in the vicinity for the periods before and after the earthquake, and thus we used the NEIC's PDE catalog, which is only complete at and above magnitude 4.5 (Fig. 7b). Albeit few, the aftershocks are clearly more abundant at the eastern terminus of the fault (Fig. 7a), consistent with our hypothesis that dynamically triggered seismicity rate increase should have the same asymmetry as that predicted by directive rupture propagation. This earthquake does not provide a good discriminant between the efficiency of static and dynamic stress changes as triggering agents, as the most significant slip occurs at the center of the fault and extends primarily eastward.

**2000  $M_w$  8.1 Papua, New Guinea.** Asymmetric radiation of dynamic deformations is observed in teleseismic body waves from this earthquake, suggesting a similar pattern at aftershock distances. To date the only available analysis of this earthquake is the unpublished result of Yagi and Kikuchi (2000a) posted on their web site. From a model based on teleseismic body waves, they inferred a vertical strike-slip event that ruptured unilaterally southward for nearly 185 km (Fig. 8a). Corroborative evidence of southward rupture propagation comes from the fact that the Harvard CMT centroid

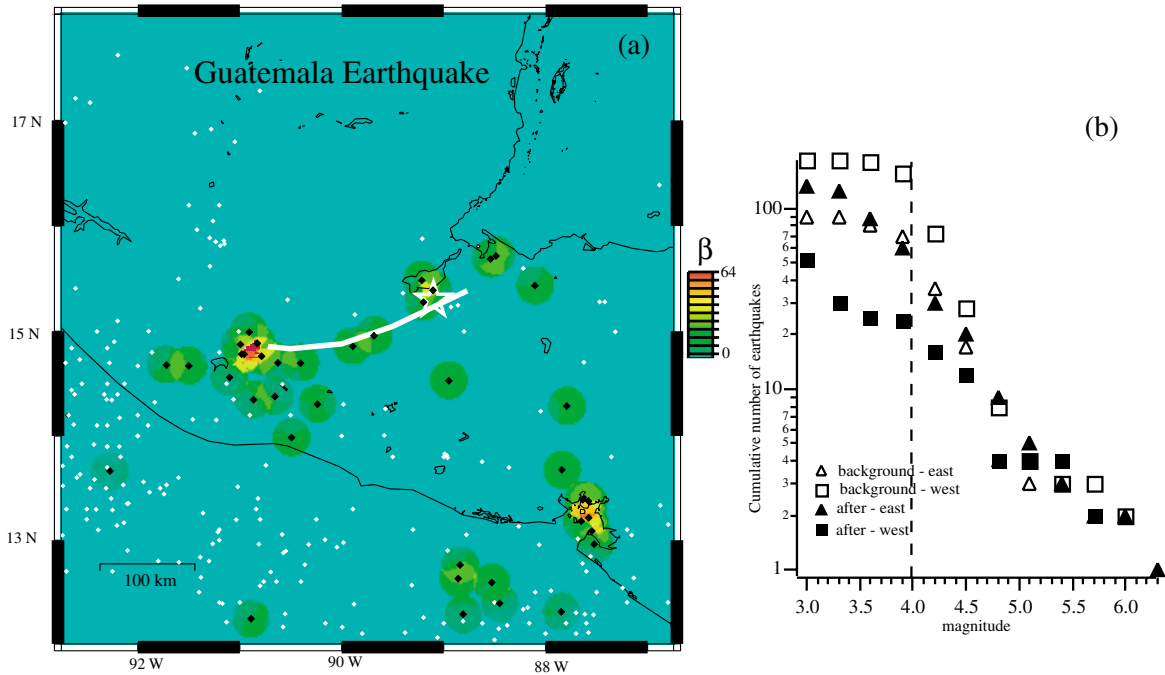


Figure 5. (a) Map of seismicity and  $\beta$ -statistic calculated for the Guatemala earthquake. We include only crustal events with focal depths less than 40 km. (b) Cumulative number of earthquakes in the time period and geographic region surrounding the Guatemala earthquake (see Table 2). The seismicity in (a) is sparse because the catalog is complete only above magnitude 4.0. Accordingly, we used a smoothing radius of 20 km and  $t_a = 120$  days. See Figure 2 caption for further details.

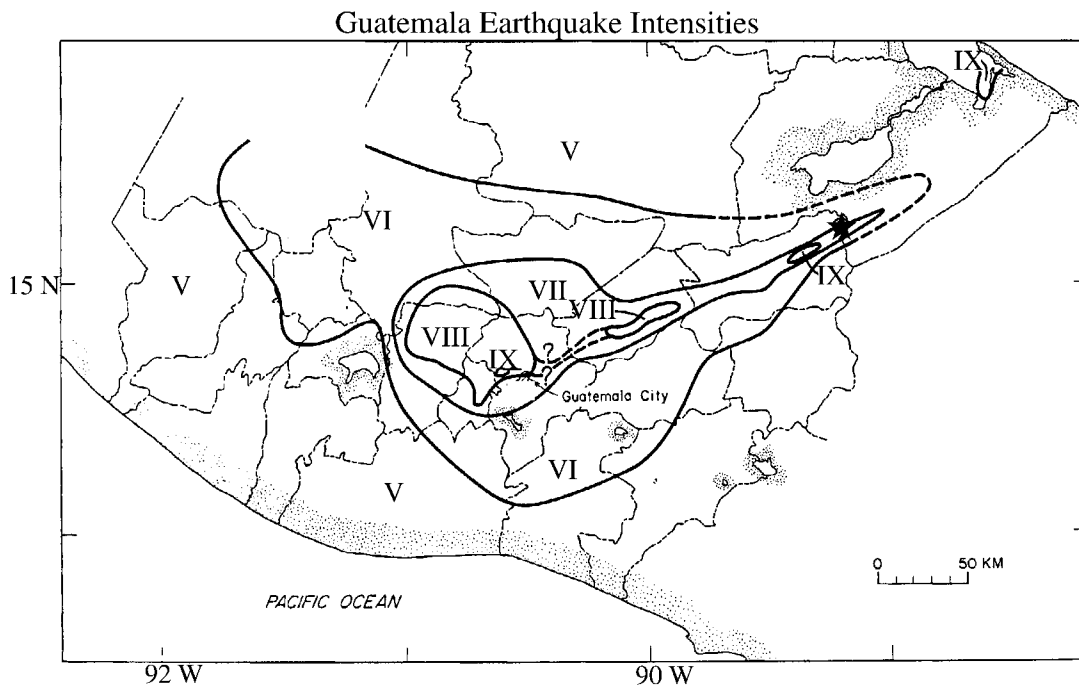


Figure 6. Isoseismal map for the Guatemala earthquake, from Espinosa *et al.* (1976). The star shows the approximate location of the epicenter. The fault trace trends approximately east-west along the axis of the isoseismal shapes. Note the asymmetric pattern of isoseismals, indicating greater shaking levels toward the west end of the rupture.

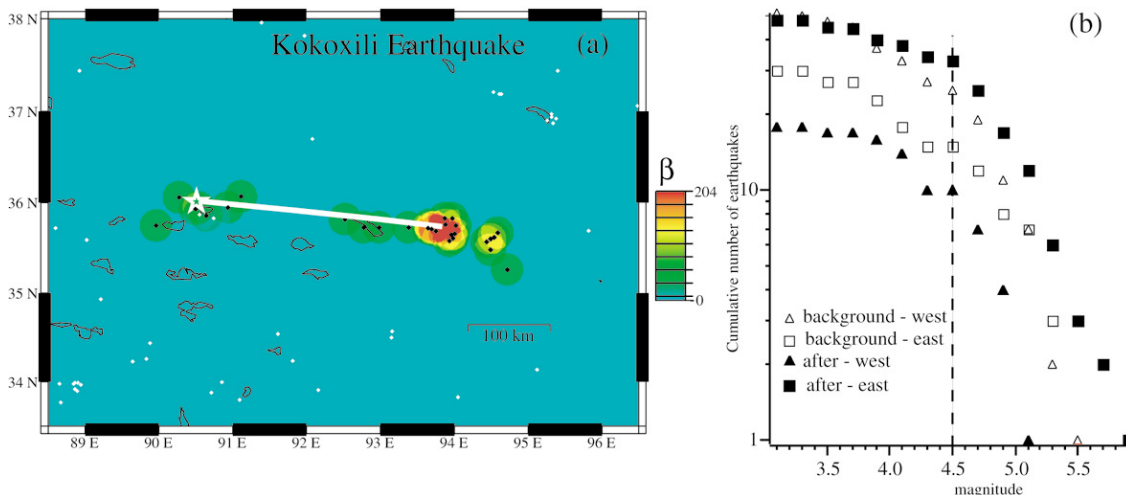


Figure 7. (a) Map of the seismicity and  $\beta$ -statistic calculated for the Kokoxili, China, earthquake using the PDE catalog with smoothing radius of 20 km. (b) Cumulative number of earthquakes in the time period and geographic region surrounding the Kokoxili earthquake (see Table 2). See Figure 2 caption for further details.

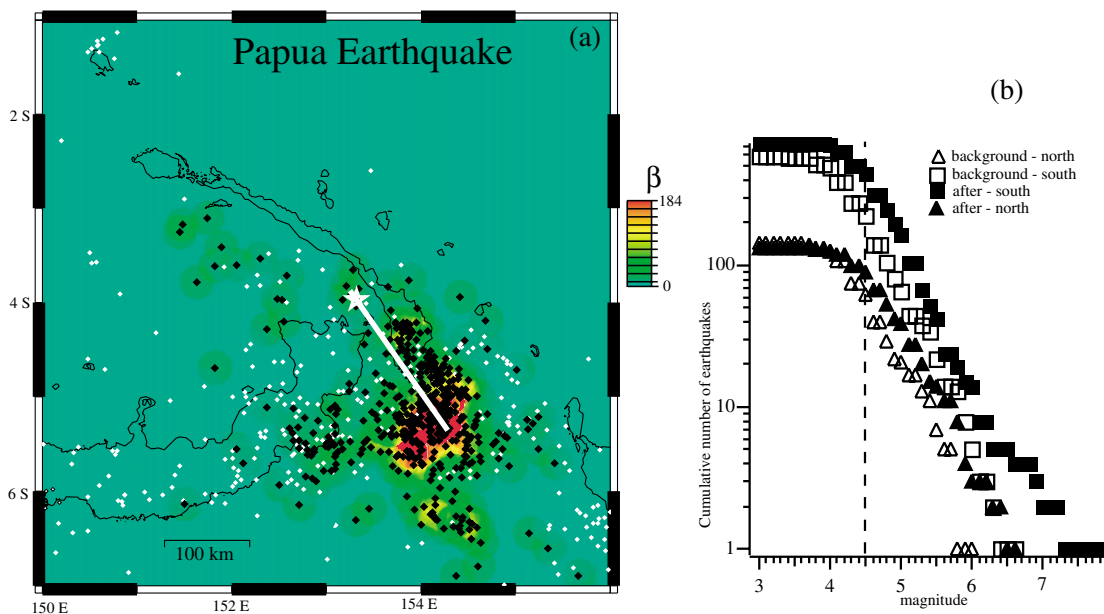


Figure 8. (a) Map of the seismicity and  $\beta$ -statistic calculated for the Papua New Guinea earthquake using the PDE catalog with smoothing radius of 20 km. (b) Cumulative number of earthquakes in the time period and geographic region surrounding the Papua New Guinea earthquake (see Table 2). See Figure 2 caption for further details.

location (Dziewonski *et al.*, 1981; Ekström, 1994) is offset southward from the epicenter by approximately 90 km.

To our knowledge no local network and catalog exist in the vicinity of New Guinea, so we used the NEIC’s PDE catalog. All background events are smaller than  $M$  6.5. The  $\beta$ -map and seismicity reveal a prominent rate increase at and more than 100 km beyond the southern end of the fault, consistent with our hypothesis. Most of this activity occurred within the first few days following the mainshock. Some of

the aftershocks at the southern end of the fault undoubtedly are secondary aftershocks of the  $M$  7.8 and  $M$  7.2 events that occurred close to the southern end of the rupture within the first 24 hr after the mainshock.

The static stress field inferred from the unpublished slip distribution derived by Yagi and Kikuchi (2000a) may share the same asymmetry as the seismicity rate change pattern and thus may correlate equally well with the seismicity rate change pattern. Yagi and Kikuchi (2000a) noted the maxi-

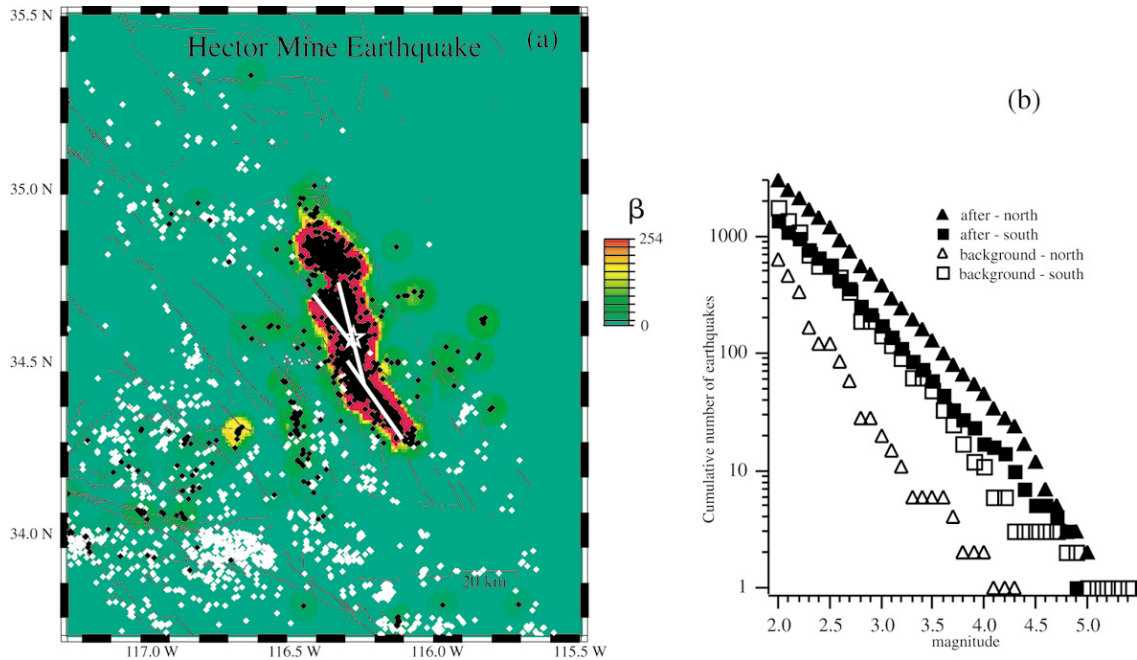


Figure 9. (a) Map of the seismicity and  $\beta$ -statistic calculated for the Hector Mine earthquake. (b) Cumulative number of earthquakes in the time period and geographic region surrounding the Hector Mine earthquake (see Table 2). See Figure 2 caption for further details.

mum slip occurs approximately 130 km from the hypocenter and extends primarily southward along the remaining third of the rupture surface.

**1999 M 7.1 Hector Mine, California.** The rupture history of this bilateral, strike-slip earthquake was complex (Dreger and Kaverina, 2000; Ji *et al.*, 2002) (Fig. 9a). Nonetheless, as noted before, the Hector Mine rupture is considered directive because greater moment release is presumed to have occurred on the longer rupture segment. Remote triggering consistent with our hypothesis has already been documented (Gomberg *et al.*, 2001), so here we focus on the rate change at aftershock distances. We use the CNSS catalog and choose a background period free of  $M > 5.5$  earthquakes (i.e., ending before the 1992 Joshua Tree earthquake; Table 2 and Fig. 9b). The aftershock distribution is clearly inconsistent with our hypothesis (Fig. 9a). As noted in Scientists from the U.S. Geological Survey *et al.* (2000), there was a more vigorous increase in seismicity immediately north of the rupture than south of it. This picture is complicated, however, by the presence of secondary aftershocks associated with an  $M 5.8$  aftershock at the northern end of the rupture minutes after the mainshock and an  $M 5.7$  aftershock along the southernmost rupture segment.

**1999 M 7.4 Izmit, Turkey.** The surface dynamic displacement field associated with this earthquake has been sampled at local and teleseismic distances. A number of rupture models have been derived for the Izmit earthquake, constrained

by local seismic data (Bouchon *et al.*, 2000) and by teleseismic waveforms, both alone and combined with interferometric synthetic aperture radar images (Yagi and Kikuchi [1999] and DeLouis *et al.* [2000], respectively). These data and models show the event to be a bilateral, yet still directive, nearly vertical strike-slip rupture, with more moment released along the longer fault zone, east of the hypocenter (Table 1; Fig. 10a).

The local seismicity appears consistent with our hypothesis, with two regions of pronounced rate change east of the hypocenter (Fig. 10a). We computed  $\beta$  for a catalog obtained from the Kandilli Observatory in Turkey (Table 2) using only observations before the 12 November 1999  $M 7.2$  Duzce earthquake (Fig. 10a), so that its aftershocks are not included in the rate change estimates.

The Izmit earthquake sequence highlights the need to consider the background seismicity when making inferences about how a mainshock changes the seismicity rate. Figure 10 shows that the background rate was higher west of the hypocenter than east of it. Hence, while the aftershock rates are similar east and west of the epicenter, and an intense cluster of aftershocks occurred west of the rupture, the rate *increase* is greatest to the east.

The Izmit earthquake allows us to compare qualitatively the correlation of rate change with both the static and dynamic stress changes. The change in the static Coulomb failure stress, or  $\Delta CFS$ , as shown in Parsons *et al.* (2000), is relatively symmetric, with regions of highest positive stress changes at either end of the fault (Fig. 10c). Parsons *et al.*

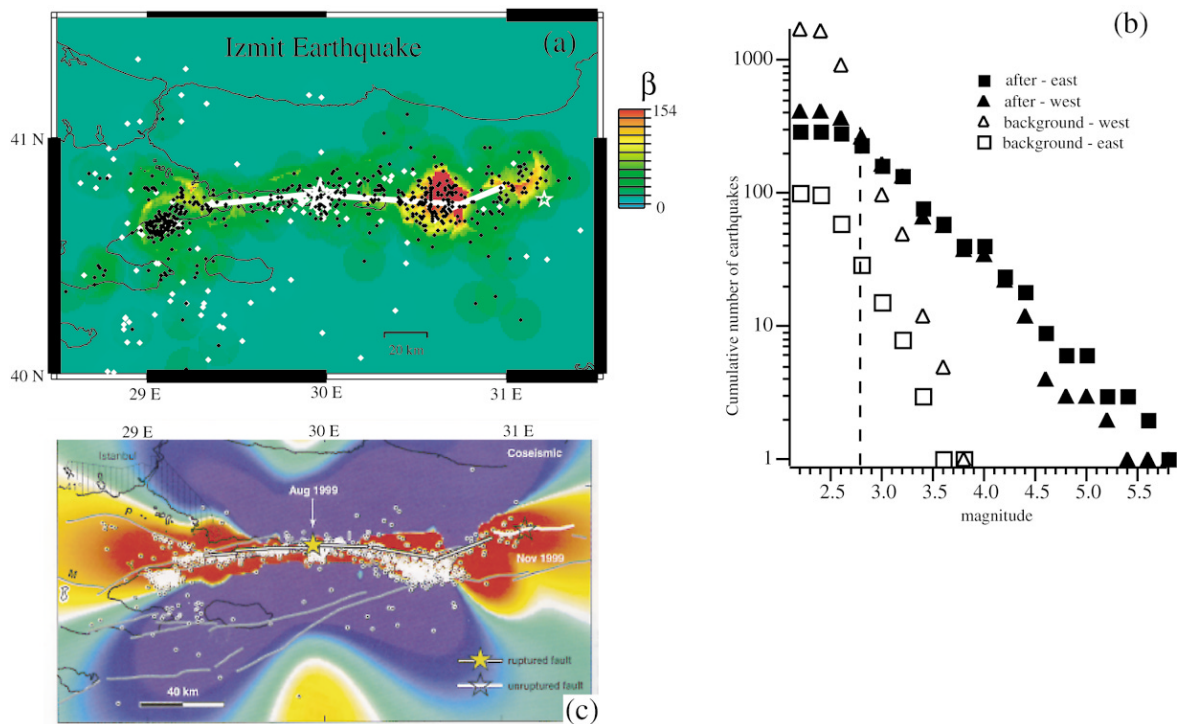


Figure 10. (a) Map of the seismicity and  $\beta$ -statistic calculated for the Izmit earthquake. The white star near the east end of the rupture is the epicenter of the  $M_w$  7.2 Duzce earthquake, which occurred 87 days after the Izmit event. (b) Cumulative number of earthquakes in the time period and geographic region surrounding the Izmit earthquake (see Table 2). (c) Calculated static Coulomb stress changes (color shaded) and aftershock epicenters (small white circles), from Parsons *et al.* (2000). Color coding saturates at  $\pm 0.1$  MPa. See Figure 2 caption for further details.

(2000) compared  $\Delta$ CFS to the distribution of aftershocks and noted that most aftershocks occurred in regions of Coulomb stress increase. However, the  $\Delta$ CFS map they show does not have the asymmetry apparent in the change in seismicity rate. We suggest that the asymmetry in seismicity increase was more likely produced by an asymmetry in the dynamic deformations expected for an eastward directive rupture.

**2001 M 6.6 Tottori, Japan.** Strong-motion and teleseismic seismic data suggest a focusing of dynamic deformations toward the southeast end of the fault. Using a waveform inversion technique, Yagi and Kikuchi (2000b) show on their web site a slip model with greatest slip along the southeast rupture segment (Fig. 11a). The epicenter determined by the JMA is in the center of the rupture (Fig. 11a). Although the Harvard CMT centroid ( $35.41^\circ$  N,  $133.23^\circ$  E) (Dziewonski *et al.*, 1981; Ekström, 1994) is near the northern end of the distribution of aftershocks, suggesting a northward-directed rupture, the evidence of Yagi and Kikuchi (2000b) provide stronger evidence of southward directivity.

We use the JMA catalog to estimate the seismicity rate change (Fig. 11b; Table 2). The rate change pattern and the inferred southward direction of rupture are inconsistent with our hypothesis, as the region of greatest seismicity increase is north of the hypocenter. The linear patch of rate increase

parallel and approximately 30 km west of the rupture begins to develop 47 hr after the Tottori event with an  $M$  5.5 earthquake at the southern end of the lineation. Understanding the relationship of this to the Tottori earthquake will require additional study to explain both its spatial relationship to the Tottori mainshock and the 47 hr time delay.

**1995 M 6.9 Kobe, Japan.** According to our criteria, the Kobe earthquake was not directive. Wald (2001) models the Kobe earthquake faulting as a nearly vertical strike-slip event, with 40% of the slip along a 40-km-long fault extending northeast of the hypocenter and the remaining 60% of the slip along a shorter fault extending southwest. Wald's analysis (2001) is based on near- and far-field seismic data and a slip history derived from them and geodetic observations.

Asymmetry in the seismicity rate change is not apparent in the  $\beta$ -map (Fig. 12a), consistent with the nondirective rupture and lack of a clear direction of focusing of radiated energy. Toda *et al.* (1998) compared the distribution of aftershocks of the Kobe earthquake to the pattern of static stress changes. To facilitate comparison with their results, we use the same catalog they used and also verify that the rate change pattern is not influenced by detection differences (Fig 12b). Toda *et al.* (1998) note that the area of increased

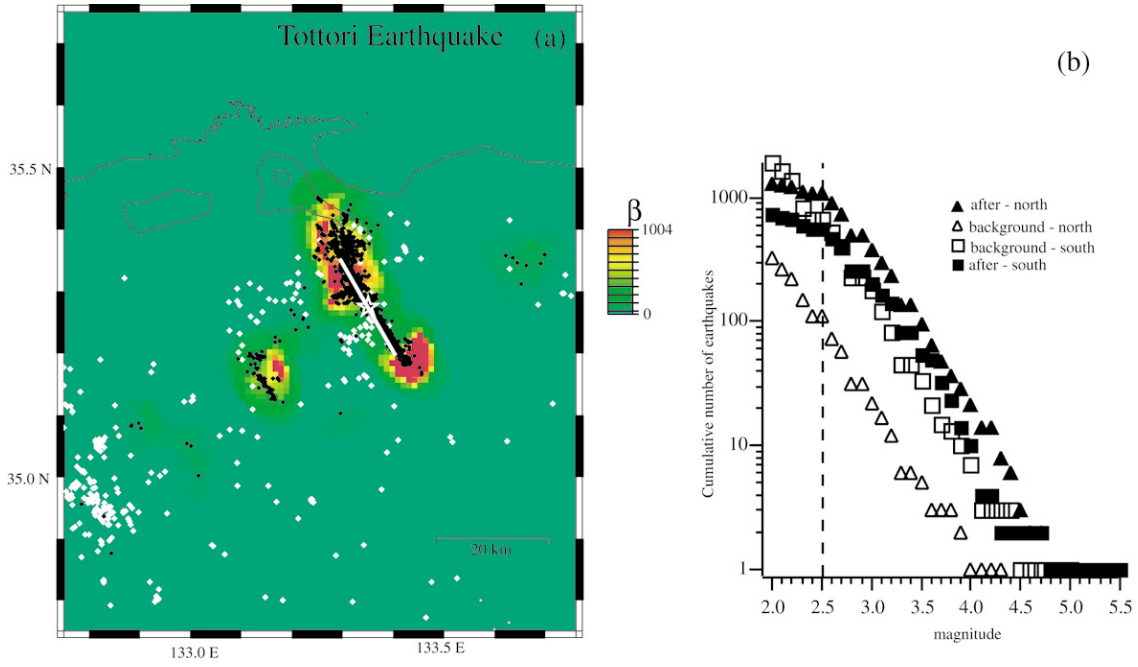


Figure 11. (a) Map of the seismicity and  $\beta$ -statistic calculated for the Tottori earthquake. (b) Cumulative number of earthquakes in the time period and geographic region surrounding the Tottori earthquake (see Table 2). The white star is the epicenter determined by JMA. See Figure 2 caption for further details.

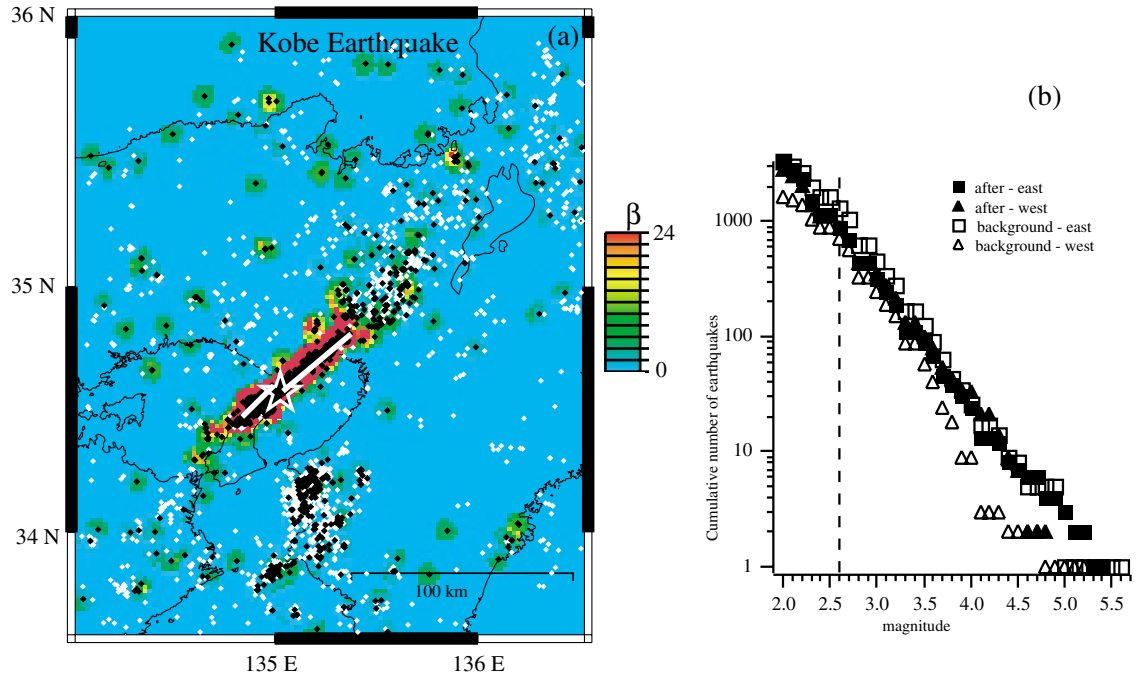


Figure 12. (a) Map of the seismicity and  $\beta$ -statistic calculated for the Kobe earthquake. (b) Cumulative number of earthquakes in the time period and geographic region surrounding the Kobe earthquake (see Table 2). The portion of the JMA catalog used is the same as in Toda *et al.* (1998) and includes only  $M \geq 2.6$  events in the depth range 0–30 km. The figure format is the same as for Figure 2.

seismicity rate off the northern end of the rupture is larger than that off the southern end and that activity increased after the mainshock southeast of the southern fault (Fig. 12c). They also note that the areas northeast and south of the rupture were active prior to the earthquake, an observation that is evident in Figure. 12a. In contrast to Toda *et al.* (1998), we do not find a significant increase in activity in these areas because we use a more conservative measure of rate change. Toda *et al.* (1998) calculate the ratio of mean rates before and after the earthquake, a method that does not take into account the expected intrinsic variation in rate, which the  $\beta$ -statistic does account for. We suggest that use of the  $\beta$ -statistic is more conservative and avoids ascribing significance to rate changes due to intrinsic fluctuations in earthquake activity unrelated to a mainshock.

**1999 M 7.0 Tehuacan, Mexico.** Both regional waveform observations and the distribution of intensities indicate that this westward-dipping, normal-faulting earthquake was directive to the northwest (Singh *et al.*, 1999). A finite source model has not been published, so we estimate a 53-km fault length using the relations of Wells and Coppersmith (1994). Unfortunately the location of the rupture surface relative to the hypocenter is unknown (i.e., whether it was unilateral or bilateral, Fig. 13a).

We use the catalog produced by the Servicio Sismológico Nacional de Mexico to estimate the rate change pattern. Because the aftershock rate was low for an event of

this magnitude (Singh *et al.*, 1999) and  $M_{\min}$  is high, relatively few earthquakes in the catalog are available for estimating the coseismic rate change. Although precise rates cannot be estimated, the lack of events in the background period suggests the number of earthquakes in the after period is unusual and undoubtedly related to the Tehuacan earthquake. However, the lack of information about the rupture dimensions and location relative to the hypocenter (Fig. 13a) make it impossible to test our hypothesis. Although the Singh *et al.* (1999) analyses show the earthquake was directive to the northwest, the most significant rate increase (a cluster of four aftershocks) may locate either in the middle of the rupture or off the northern end. In the former case, the seismicity is inconsistent with our hypothesis, and in the latter case, it is consistent.

**1983 M 7.3 Borah Peak, Idaho.** The Borah Peak earthquake is perhaps the largest normal-faulting event with a catalog complete to magnitudes as low as  $M$  3.0 (Fig. 14a). Evidence for a strongly directive rupture to the north comes from teleseismic  $P$ -wave observations (Mendoza and Hartzell, 1988). An isoseismal map for this earthquake (Fig. 15) shows higher intensities extending farther to the north, presumably indicative of larger ground motions and northward directivity. This is particularly true at greater distances, where the modified Mercalli intensity II–IV isoseismals reflect an average over a large area, so that site conditions should not bias the pattern. A northward-propagating rupture

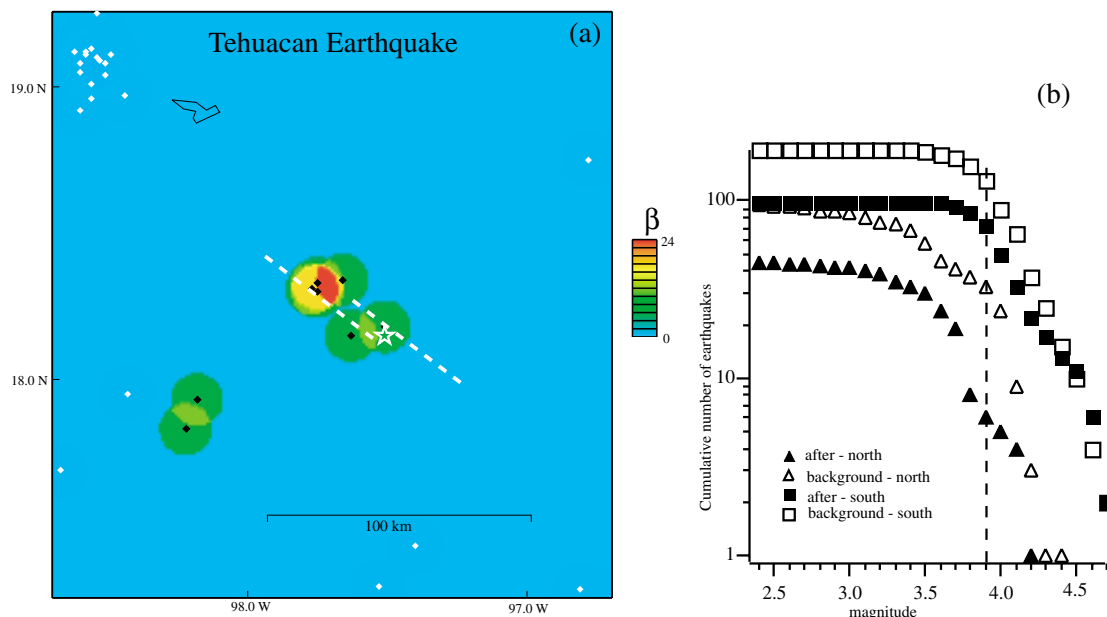


Figure 13. (a) Map of the seismicity and  $\beta$ -statistic variations calculated for the Tehuacan earthquake. A smoothing radius of 10 km was used to derive the  $\beta$ -map. Dashed lines indicate the probable range of the length, strike, and location of a line intersecting a horizontal plane at the hypocenter and rupture surface. (b) Cumulative number of earthquakes in the time period and geographic region surrounding the Tehuacan earthquake (see Table 2). See Figure 2 caption for further details.

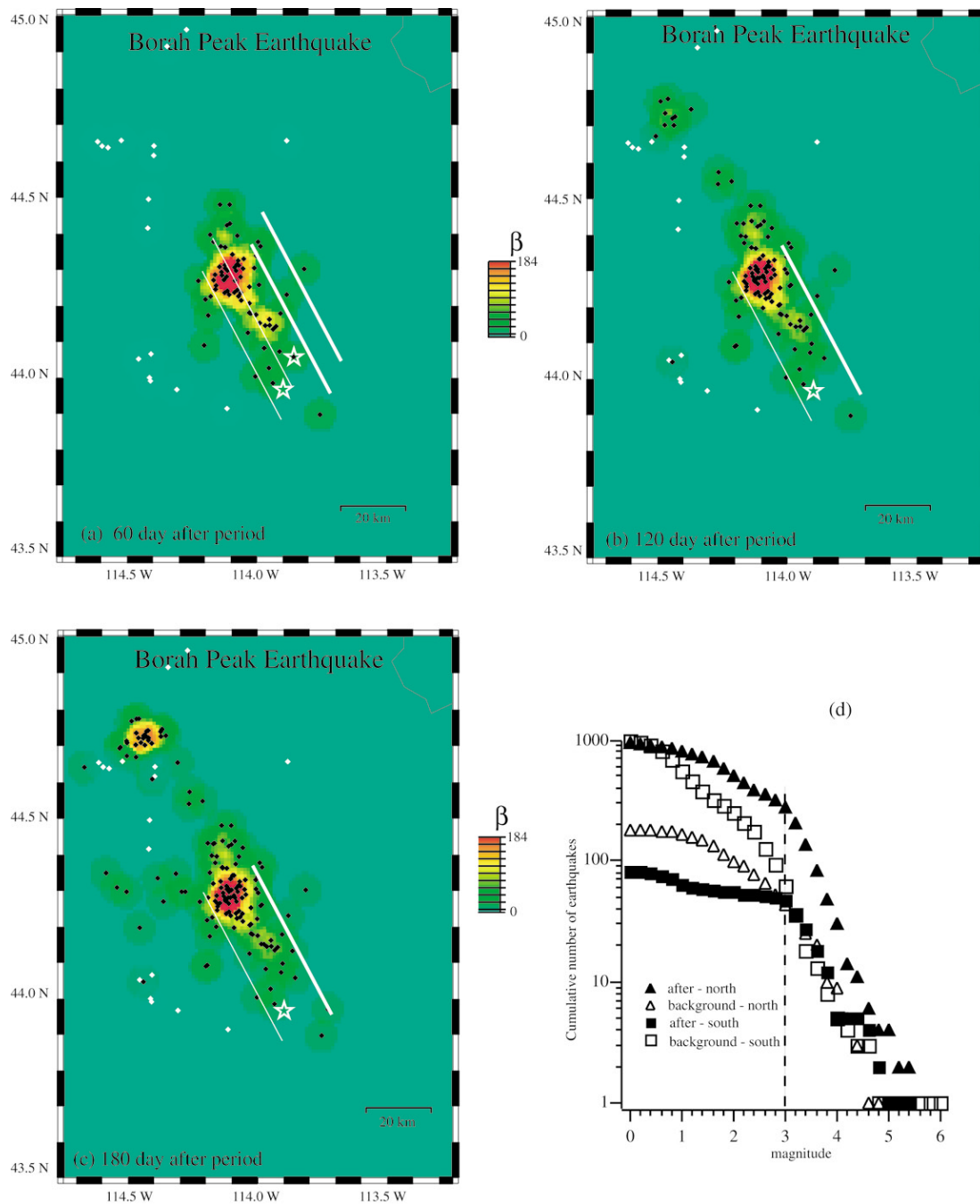


Figure 14. Maps of the seismicity and  $\beta$ -statistic calculated for the Borah Peak earthquake. Thick and thin parallel white lines show the surface trace and bottom, respectively, of proposed rupture planes. (a) The more westerly rupture plane and epicenter (star) correspond to the hypocenter reported in the CNSS catalog; the eastern rupture plane and epicenter are taken from Richins *et al.* (1987). We assume the latter is correct (see text) and use it in subsequent figures and in interpretations. The after period is  $t_a = 60$  days. (b) Same as (a) except  $t_a = 120$  days. (c) Same as (a) except  $t_a = 180$  days. (d) Cumulative number of earthquakes in the time period and geographic region surrounding the Borah Peak earthquake (see Table 2). See Figure 2 caption for further details.

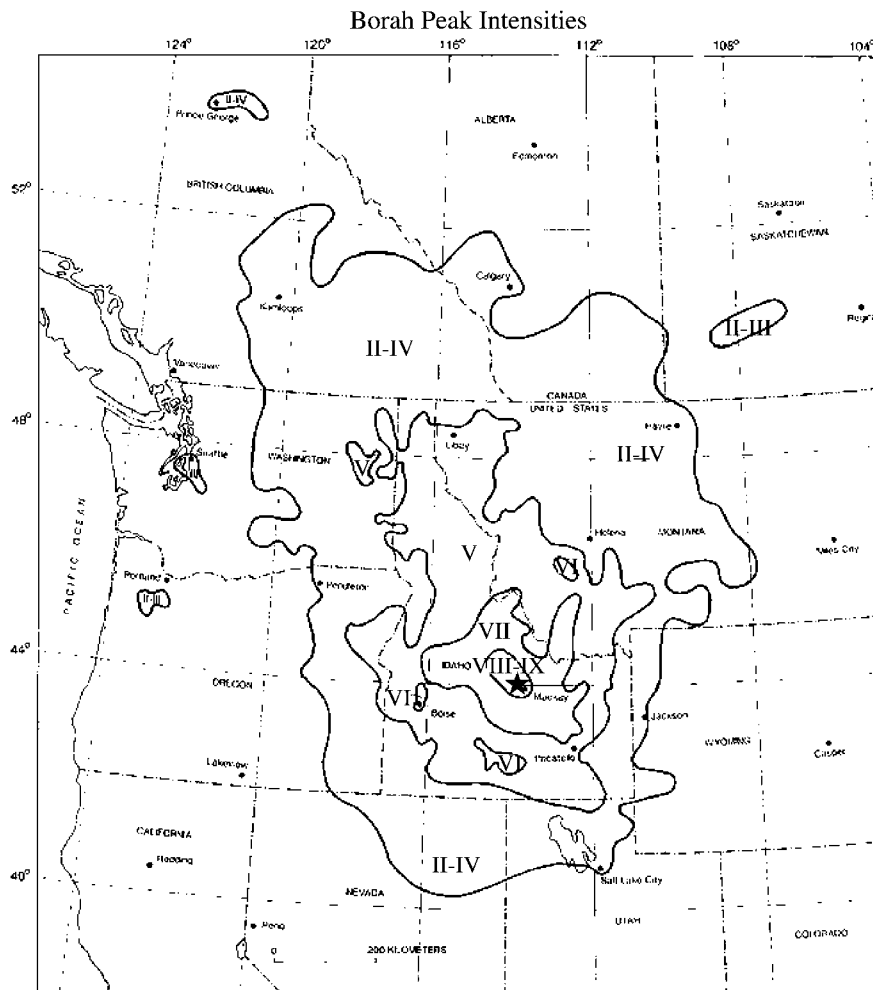


Figure 15. Isoseismal map for the Borah Peak earthquake, from Stover and Coffman (1993). The star shows the approximate location of the epicenter. Note the asymmetric pattern, indicating greater shaking levels toward the north.

is also implied by the geometry of the hypocenter relative to the extent of faulting (approximately 85% of the rupture length is north of the hypocenter), although two different hypocenters and fault locations are reported in the literature. Richins *et al.* (1987) reported a hypocenter to the southwest of the location reported in the CNSS catalog and in Mendoza and Hartzell (1988). The Richins *et al.* (1987) hypocenter and fault geometry are more consistent with the observed surface rupture and with the immediate aftershocks, assuming that most of these events lie along the rupture plane (Fig 14a).

We use the CNSS catalog to estimate the pattern of seismicity rate change (Fig. 14d). The change in seismicity rate during the first 60 days after the mainshock is clearly greatest at the northern end of the fault and perhaps extends somewhat beyond this end, consistent with our dynamic triggering hypothesis. The highly asymmetric pattern in the  $\beta$ -map apparently extends approximately 1 rupture length beyond the northwest end of the rupture. Du *et al.* (1992) inferred

the maximum slip at approximately 30 km from the northern end of the fault, or approximately centered between the hypocenter and northern fault end. This may produce an asymmetric static stress change, although it is unclear why it would have an effect on the seismicity that extends only northward and well off the fault.

Although we do not consider the temporal behavior of seismicity rate changes, we comment on an interesting feature of the post-Borah Peak seismicity as fodder for future studies. The asymmetry in rate change following the Borah Peak earthquake evolved slowly in an apparently expanding area away from the northern end of the rupture (Figs. 14a-c). Most of the earthquakes constituting this growing rate increase are probably not secondary aftershocks because all have  $M < 4.5$ . Such a delayed (or slowly evolving) and expanding rate change is not consistent with most physical models invoked to explain the temporal behavior of aftershocks (e.g., Dieterich, 1994). It was not observed for any of the other earthquakes we studied.

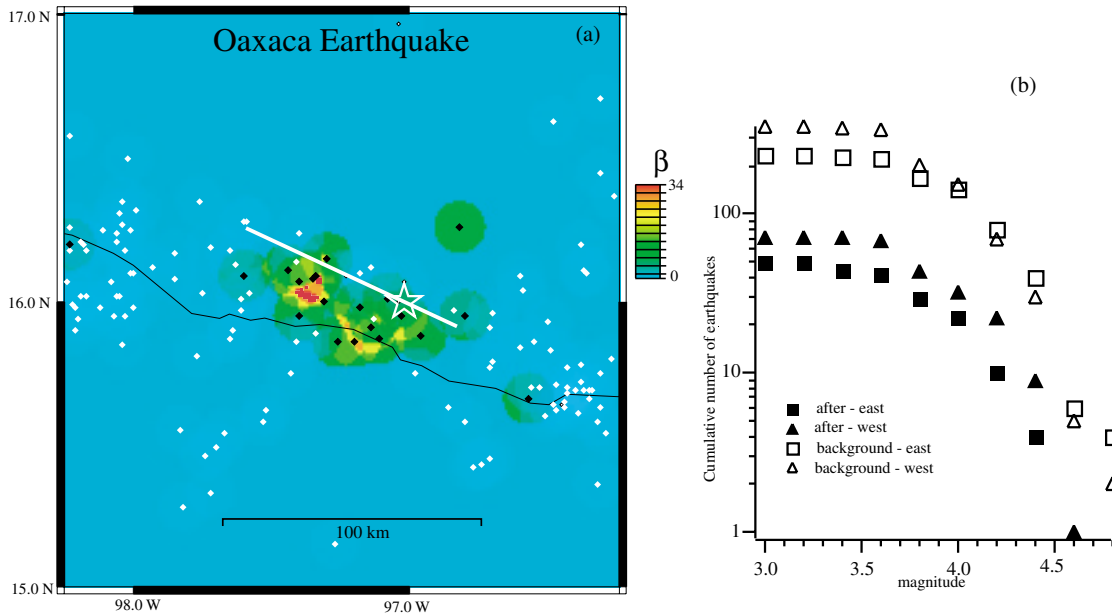


Figure 16. (a) Map of the seismicity and  $\beta$ -statistic calculated for the Oaxaca earthquake. The white line shows the intersection of a horizontal surface at the hypocenter's depth with the rupture surface. (b) Cumulative number of earthquakes in the time period and geographic region surrounding the Oaxaca earthquake (see Table 2). See Figure 2 caption for further details.

*1999 M 7.5 Oaxaca, Mexico.* Local and teleseismic displacement seismograms and isoseismals show that the rupture of this normal-faulting, northeast-dipping earthquake propagated northwesterly (Singh *et al.*, 2000) (Fig. 16a). A slip history determined from strong-motion waveform modeling also shows this to be a directive rupture to the northwest (Hernandez *et al.*, 2001).

To estimate the rate change pattern we use the catalog produced by the Servicio Seismológico Nacional de Mexico. According to the  $\beta$ -map and seismicity distribution, the greatest rate change occurred along the center of the rupture in the same general vicinity as the maximum slip inferred by Hernandez *et al.* (2001). These observations are not consistent with our hypothesis.

### Summary and Conclusions

We have compared the patterns of seismicity rate change produced by 15 earthquakes with the corresponding inferred dynamic deformation fields. While the dynamic deformation fields were measured directly, these measurements were typically sparsely distributed at the surface and often located at some distance from the putatively triggered seismicity. We have employed additional information and slip history models to infer the relative amplitudes of the dynamic deformations at seismogenic depth. We have focused on earthquakes whose dynamic deformation fields were likely asymmetric owing to focusing associated with the directivity of their ruptures. Because rupture directivity affects only the dynamic deformations, our analysis has the

potential to distinguish between the roles of static and dynamic stresses in the triggering process.

Of the nine earthquakes with unilateral rupture in our study, eight produced greater near-field seismicity rate increase in the direction of focusing than in the opposite direction, consistent with our hypothesis (Table 3). This group of events includes one normal- and eight strike-slip-faulting earthquakes. The inconsistent case is the Superstition Hills earthquake, which was preceded (by 11 hr) by a conjugate earthquake of magnitude large enough to contribute significantly to the rate change (and perhaps rupture process) associated with the Superstition Hills event. Our result for the (unilaterally rupturing) Gulf of Aqaba earthquake is ambiguous, due to data limitations. However, other studies suggest that it, too, is consistent with the hypothesis.

For the five earthquakes with bilateral rupture that we studied, the results are mixed (Table 3). For these events, we have some doubt about our ability to assess the directionality of the dynamic deformations. In a unilateral rupture, the propagation and thus the focusing are always in one direction, regardless of the complexity of the slip distribution in time and space. But for bilateral ruptures, factors other than the net moment release and segment length (e.g., the distribution of slip with depth, changes in rheology over the fault surface, and variations in propagation velocity) may influence the focusing and net directionality of dynamic deformations.

Overall, the correlation between seismicity rate change and rupture dynamics decreases as the rupture complexity or uncertainty grows. In the cases with clearly directive

Table 3  
Correlation Summary

Rupture Type	Earthquake	Rupture Segmentation	Magnitude	Consistency of Rate Change Symmetry, Distance Range		Comment
				Near	Far	
Directive strike slip	Coyote Lake (1979)	Unilateral	$M_s$ 5.7	Yes		Preceded by $M_w$ 6.1 conjugate event Catalog analysis inconclusive, published studies suggest consistency with hypothesis  Seismicity rate low because of high completion magnitude Seismicity rate low because of high completion magnitude
	Superstition Hills (1987)		$M_w$ 6.6	No		
	Gulf of Aqaba (1995)		$M_w$ 7.3	Yes?	Yes?	
	Landers (1992)		$M_w$ 7.3	Yes	Yes	
	Guatemala (1976)		$M_s$ 7.5	Yes		
	Kokoxili, China (2001)		$M_w$ 7.8	Yes		
	Papua New Guinea (2000)		$M_w$ 8.1	Yes		
	Antarctic (1998)		$M_w$ 8.1	Yes		
Maybe directive	Tottori (2000)	Bilateral	$M_w$ 7.1	No	Yes	Rupture history preliminary, parameters inconsistent?
	Not directive		Kobe (1995)	$M_w$ 6.9	Yes	
Directive dip slip	Tehuacan (1999)	Unknown	$M_w$ 7.0	?		Seismicity rate low because of high completion magnitude, fault location imprecisely known  Seismicity rate low with respect to completion magnitude
	Borah Peak (1983)	Unilateral	$M_w$ 7.3	Yes		
	Oaxaca (1999)	Bilateral	$M_w$ 7.5	No		

Summary of analysis results for the 13 earthquakes we studied combined with published results for some of these events at remote distances and two additional earthquakes. A “yes” in the columns labeled “Consistency of Rate Change Symmetry” indicates the most significant seismicity rate increase was in the direction of inferred focusing of dynamic deformations. Unilateral ruptures (third column) are those in which one rupture segment contains >80% of the total rupture length.

mainshocks, observed asymmetries in seismicity rate change are consistent with the inferred direction of maximum radiated dynamic deformations. In particular, the rate change associated with eight of the nine unilateral ruptures, as well as for the most clearly directive bilateral rupture (the Izmit earthquake), are consistent with our hypothesis. We suggest that this agreement may be evidence for near-field dynamic triggering.

The earthquakes we studied that lack correlation between rupture directionality and seismicity rate change may also be informative. In the case of the Kobe earthquake, where both the rupture history and seismicity rate change are well constrained, the rupture is not clearly directive and the rate change shows no pronounced asymmetry, as our hypothesis would predict. However, for the Hector Mine earthquake, rupture history and rate change are also well constrained, but inconsistent with our hypothesis. The Tottori and Oaxaca earthquakes also yield a negative result with respect to our hypothesis; the observations used for these earthquakes have the greatest uncertainties of those studied.

For the Coyote Lake, Izmit, and Borah Peak earthquakes, we were able to compare qualitatively the seismicity rate changes with both (inferred or published) static stress changes in simple elastic models and the dynamic defor-

mation fields. In these cases, areas of rate increase largely coincide with regions of static Coulomb stress increase. However, in each case an asymmetric component in the rate change pattern is present that cannot be as easily explained by the static stress change pattern. These observations are consistent with Kilb *et al.* (2000), who found that for the (unilaterally rupturing) Landers earthquake the (asymmetric) seismicity rate change pattern correlates better with the dynamic deformations than with the pattern of static stress changes. The dynamic triggering inferred in this study occurs primarily in what is traditionally referred to as the aftershock zone, where the post-mainshock seismicity increase has most often been attributed to mainshock-generated static stress changes. Our observations do not imply that static stress changes play no role in earthquake triggering, or even a minor role. Rather, they suggest that both static and dynamic stresses associated with mainshocks contribute to the triggering of aftershocks.

Finally, we believe that our results dispel the notion that dynamic triggering is a phenomenon confined to remote distances and geothermal regions. Among the seven or eight directive earthquakes for which a positive correlation is observed, the most significant triggered rate changes occurred in areas not known to be geothermal or volcanic.

## Acknowledgments

We thank Shinji Toda for the JMA Tottori catalog and Javier Pacheco for the Servicio Seismologico Nacional de Mexico catalog. Russell Robinson, Andy Michael, Jeanne Hardebeck, Götz Bokelmann, and an anonymous reviewer provided helpful very helpful reviews. CERI Contribution Number 467.

## References

- Aki, K. and P. G. Richards (1980). *Quantitative Seismology, Theory and Methods*, Vol. 2, W. H. Freeman, San Francisco.
- Boore, D. M. and W. B. Joyner (1978). The influence of rupture incoherence on seismic directivity, *Bull. Seism. Soc. Am.* **68**, 283–300.
- Bouchon, M. (1982). The rupture mechanism of the Coyote Lake earthquake of 6 August 1979 inferred from near-field data, *Bull. Seism. Soc. Am.* **72**, 745–757.
- Bouchon, M., N. Toksoz, H. Karabulut, M. Brown, M. Dietrich, M. Aktar, and M. Edie (2000). Seismic imaging of the 1999 Izmit (Turkey) rupture inferred from the near-fault recordings, *Geophys. Res. Lett.* **27**, 3013–3016.
- Brodsky, E. E., V. Karakostas, and H. Kanamori (2000). A new observation of dynamically triggered regional seismicity: earthquakes in Greece following the August, 1999 Izmit, Turkey earthquake, *Geophys. Res. Lett.* **27**, 2741–2744.
- DeLouis, B., P. Lundgren, J. Salichon, and D. Giardina (2000). Joint inversion of InSAR and teleseismic data for the slip history of the 1999 Izmit (Turkey) earthquake, *Geophys. Res. Lett.* **27**, 3389–3392.
- Dieterich, J. (1994). A constitutive law for rate of earthquake production and its application to earthquake clustering, *J. Geophys. Res.* **99**, 2601–2618.
- Dreger, D. and Kaverina, A., (2000). Seismic remote sensing for the earthquake source process and near-source strong shaking: a case study of the October 16, 1999 Hector Mine earthquake, *Geophys. Res. Lett.* **27**, 1941–1944.
- Du, Y., A. Aydin, and P. Segall (1992). Comparison of various inversion techniques as applied to the determination of a geophysical deformation model for the 1983 Borah Peak earthquake, *Bull. Seism. Soc. Am.* **82**, 1840–1866.
- Dziewonski, A. M., T.-A. Chou, and J. H. Woodhouse (1981). Determination of earthquake source parameters from waveform data for studies of global and regional seismicity, *J. Geophys. Res.* **86**, 2825–2852.
- Eberhart-Phillips, D., and A. J. Michael (1998). Seismotectonics of the Loma Prieta, California, region determined from three-dimensional Vp, Vp/Vs, and seismicity, *J. Geophys. Res.* **103**, 21,099–21,120.
- Ekström, G. (1994). Rapid earthquake analysis utilizes the internet, *Comput. Phys.* **8**, 632–638.
- Espinosa, A. F., R. Husid, and A. Quesada, (1976). Intensity distribution and source parameters from field observations. The Guatemala earthquake of February 4, 1976, a preliminary report, *U.S. Geol. Surv. Profess. Pap.* **1002**, 52–66.
- Frankel, A., and L. Wennerberg, (1989). Rupture process of the  $M_s$  6.6 Superstition Hills earthquake determined from strong motion recordings: application to tomographic source inversion, *Bull. Seism. Soc. Am.* **79**, 515–541.
- Gomberg, J. (1996). Stress/strain changes and triggered seismicity following the  $M_s$  7.4 Landers, California earthquake, *J. Geophys. Res.* **101**, 751–764.
- Gomberg, J., and S. Davis (1996). Stress/strain changes and triggered seismicity at The Geysers, California, *J. Geophys. Res.* **101**, 733–749.
- Gomberg, J., P. Reasenber, P. Bodin, and R. Harris (2001). Earthquake triggering by transient seismic waves following the Landers and Hector Mine, California earthquakes, *Nature* **411**, 462–466.
- Haskell, N. (1964). Total energy and energy spectral density of elastic wave radiation from propagating faults, *Bull. Seism. Soc. Am.* **54**, 1811–1842.
- Henry, C., S. Das, and J. H. Woodhouse (2000). The great March 25, 1998, Antarctic Plate earthquake: moment tensor and rupture history, *J. Geophys. Res.* **105**, 16,097–16,118.
- Hernandez, B., N. M. Shapiro, S. K. Singh, J. F. Pacheco, F. Cotton, M. Campillo, A. Iglesias, V. Cruz, J. M. Gomez, and L. Alcántara (2001). Rupture history of September 30, 1999 intraplate earthquake of Oaxaca, Mexico ( $M_w = 7.5$ ) from inversion of strong-motion data, *Geophys. Res. Lett.* **28**, 363–366.
- Hill, D. P., P. Reasenber, A. Michael, R. Simpson, J. Brune, D. DePolo, R. Smith, S. Nava, J. Gomberg, G. Beroza, W. Arabasz, S. Walter, M. Johnston, L. Jones, W. Ellsworth, and J. Zollweg (1993). Remote seismicity triggered by the  $M$  7.5 Landers, California earthquake of June 28, 1992, *Science* **260**, 1617–1623.
- Hill, D. P., M. J. S. Johnston, J. O. Langbein, and R. Bilham (1995). Response of Long Valley caldera to the  $M_w = 7.3$  Landers, California, earthquake, *J. Geophys. Res.* **100**, 12,985–13,005.
- Hough, S. E. (2001). Triggered earthquakes and the 1811–1812 New Madrid, Central United States earthquake sequence, *Bull. Seism. Soc. Am.* **91**, 1574–1581.
- Hwang, L. J., H. Magistrale, and H. Kanamori (1990). Teleseismic source parameters and rupture characteristics of the 24 November 1987, Superstition Hills earthquake, *Bull. Seism. Soc. Am.* **80**, 43–56.
- Ji, C., Wald, D. J., and Helmberger, D.V., (2002). Source description of the 1999 Hector Mine, California, earthquake, part II: Complexity of slip history, *Bull. Seism. Soc. Am.* **92**, 1208–1226.
- Kikuchi, K., and Y. Yamanaki (2001). 2001/11/14 Qinghai Xinjiang border, China earthquake special web page, <http://www.wic.eri.u-tokyo.ac.jp/topics/200111140926/index.html>, Seismol. Note Earthquake Info. Center, Earthquake Res. Inst., Univ. of Tokyo, Japan.
- Kilb, D., Gomberg, J., and Bodin, P. (2000). Earthquake triggering by dynamic stresses, *Nature* **408**, 570–574.
- Kilb, D., Gomberg, J., and Bodin, P. (2000). Aftershock triggering by complete Coulomb stresses. *J. Geophys. Res.* **107**, no. B4, 1–15.
- Klinger, Y., L. Rivera, H. Haessler, and J. Maurin (1999). Active faulting in the Gulf of Aqaba: new knowledge from the  $M_w$  7.3 earthquake of 22 November 1995, *Bull. Seism. Soc. Am.* **89**, 1025–1036.
- Larsen, S., R. Reilinger, H. Neugebauer, and W. Strange (1992). Global positioning system measurements of deformations associated with the 1987 Superstition Hills earthquake: evidence for conjugate faulting, *J. Geophys. Res.* **97**, 4885–4902.
- Liu, H., and D. V. Helmberger (1983). The near-source ground motion of the 6 August, 1979 Coyote Lake, California earthquake, *Bull. Seism. Soc. Am.* **73**, 201–218.
- Matthews, M. V., and Reasenber, P. A. (1988). Statistical methods for investigating quiescence and other temporal seismicity patterns, *Pure Appl. Geophys.* **126**, 357–372.
- McLaughlin, R. J., J. C. Clark, R. C. Jachens, A. Griscom, V. E. Langenheim, K. M. Schmidt, C. M. Wentworth, R. E. Wells, and Z. C. Valin (1999). Geology and crustal structure of the Loma Prieta earthquake epicentral region, *EOS* **80**, F40.
- Mendoza, C., and S. H. Hartzell (1988). Inversion for slip distribution using teleseismic P waveforms: North Palm Springs, Borah Peak, and Michoacan earthquakes, *Bull. Seism. Soc. Am.* **78**, 1092–1111.
- Miyake, H., T. Iwata, and K. Irikura (2001). Estimation of rupture propagation direction and strong motion generation area from azimuth and distance dependence of source amplitude spectra, *Geophys. Res. Lett.* **28**, 2727–2730.
- Mohamad, R., A. N. Darkal, D. Seber, E. Sandoval, F. Gomez, and M. Barazangi (2000). Remote earthquake triggering along the Dead Sea Fault in Syria following the 1995 Gulf of Aqaba earthquake ( $M_s = 7.3$ ), *Seismol. Res. Lett.* **71**, 47–52.
- Nettles, M., T. C. Wallace, and S. L. Beck (1999). The March 25, 1998 Antarctic plate earthquake, *Geophys. Res. Lett.* **26**, 2097–2100.
- Parsons, T., S. Toda, R. S. Stein, A. Barka, and J. H. Dieterich (2000).

- Heightened odds of large earthquakes near Istanbul: an interaction-based probability calculation, *Science* **288**, 661–665.
- Plafker, G. (1976). Tectonic aspects of the Guatemala earthquake of 4 February 1976, *Science* **193**, 1201–1208.
- Power, J. A., S. C. Moran, S. R. McNutt, S. D. Stihler, and J. J. Sanchez (2001). Seismic response of the Katmai volcanoes to the 6 December 1999 magnitude 7.0 Karluk Lake earthquake, Alaska, *Bull. Seism. Soc. Am.* **91**, 57–64.
- Protti, M., K. McNally, J. Pacheco, V. Gonzalez, C. Montero, J. Segura, J. Brenes, V. Barboza, E. Malavassi, F. Guendel, G. Simila, D. Rojas, A. Velasco, A. Mata, and W. Schillinger (1995). The March 25, 1990 ( $M_w = 7.0$ ,  $M_L = 6.8$ ), earthquake at the entrance of the Nicoya Gulf, Costa Rica: its prior activity, foreshocks, aftershocks, and triggered seismicity, *J. Geophys. Res.* **100**, 20,345–20,358.
- Richins, W. D., J. C. Pechmann, R. B. Smith, C. L. Langer, S. K. Goter, J. E. Zollweg, and J. J. King (1987). The 1983 Borah Peak, Idaho, earthquake and its aftershocks, *Bull. Seism. Soc. Am.* **77**, 694–723.
- Scientists from the U.S. Geological Survey, Southern California Earthquake Center, and California Division of Mines and Geology (2000). Preliminary report on the 16 October 1999 M7.1 Hector Mine, California, earthquake, *Seism. Res. Lett.* **71**, 11–23.
- Singh, S. K., J. G. Anderson, and M. Rodriguez (1998). Triggered seismicity in the Valley of Mexico from major earthquakes, *Geofis. Int.* **37**, 3–15.
- Singh, S. K., M. Ordaz, L. Alcantara, N. Shapiro, V. Kostoglodov, J. F. Pacheco, S. Alcocer, C. Gutierrez, R. Quaas, T. Mikumo, and E. Ovando (2000). The Oaxaca earthquake of 30 September 1999 ( $M_w = 7.5$ ): a normal-faulting event in the subducted Cocos plate, *Seism. Res. Lett.* **71**, 67–78.
- Singh, S. K., M. Ordaz, J. F. Pacheco, R. Quaas, L. Alcantara, S. Alcocer, C. Gutierrez, R. Meli, and E. Ovando (1999). A preliminary report on the Tehuacan Mexico earthquake of June 15, 1999 ( $M_w = 7.0$ ), *Seism. Res. Lett.* **70**, 489–504.
- Somerville, P. G., N. F. Smith, R. W. Graves, and N. A. Abrahamson (1997). Modification of empirical strong ground motion relations to include the amplitude and duration effects of rupture directivity, *Seism. Res. Lett.* **68**, 199–222.
- Stover, C. W., and J. L. Coffman (1993). Seismicity of the United States, 1568–1989 (Revised), *U.S. Geol. Surv. Profess. Pap.* 1527.
- Toda, S., and R. S. Stein (2000). Did stress triggering cause the large off-fault aftershocks of the 25 March 1998  $M_w = 8.1$  Antarctic plate earthquake? *Geophys. Res. Lett.* **27**, 2301–2304.
- Toda, S., Stein, R., Reasenberg, P. A., and Dieterich, J. H. (1998). Stress transferred by the 1995  $M_w = 6.9$  Kobe, Japan, shock: effect on aftershocks and future earthquake probabilities, *J. Geophys. Res.* **103**, 24,543–24,565.
- van der Woerd, J., A. S. Meriaux, Y. Klinger, F. J. Ryerson, Y. Gaudemer, and P. Tapponier (2002). The 14 November, 2001,  $M_w = 7.8$  Kokoxili earthquake in northern Tibet (Qinghai Province, China), *Seism. Res. Lett.* **73**, 125–135.
- Wald, D. J. (1996). Slip history of the 1995 Kobe, Japan, earthquake determined from strong motion, teleseismic, and geodetic data, *J. Phys. Earth* **44**, 489–503.
- Wald, D. J., and Heaton, T. H. (1994). Spatial and temporal distribution of slip for the 1992 Landers, California, earthquake, *Bull. Seism. Soc. Am.* **84**, 668–691.
- Wald, D. J., D. V. Helmberger, S. H. Hartzell (1990). Rupture process of the 1987 Superstition Hills earthquake from inversion of strong-motion data, *Bull. Seism. Soc. Am.* **80**, 1079–1098.
- Wald, D. J., D. V. Helmberger, and T. H. Heaton (1991). Rupture model of the 1989 Loma Prieta earthquake from the inversion of strong-motion and broadband teleseismic data, *Bull. Seism. Soc. Am.* **81**, 1540–1572.
- Wells, D. L., and K. J. Coppersmith (1994). New empirical relationships among magnitude, rupture length, rupture area, and surface displacement, *Bull. Seism. Soc. Am.* **84**, 974–1001.

- Yagi, Y., and K. Kikuchi (1999). Preliminary Results of Rupture Process for the 12 November 1999 Turkey Earthquake special web page, <http://www.eri.u-tokyo.ac.jp/yuji/trk2/Turkeyafter.html>, Seismol. Note Earthquake Info. Center, Earthquake Res. Inst., Univ. of Tokyo, Japan.
- Yagi, Y., and K. Kikuchi (2000a) Preliminary Results of Rupture Process for 16 November 2000 New Ireland Region, Papua special web page, <http://www.eri.u-tokyo.ac.jp/yuji/PNG/index.html>, Seismol. Note Earthquake Info. Center, Earthquake Res. Inst., Univ. of Tokyo, Japan.
- Yagi, Y., and K. Kikuchi (2000b). Source Rupture Process of the Tottoriken Seibu earthquake of 6 October 2000 special web page, <http://www.eri.u-tokyo.ac.jp/yuji/tottori/>, Seismol. Note Earthquake Info. Center, Earthquake Res. Inst., Univ. of Tokyo, Japan.
- Young, C. J., T. Lay, and C. S. Lynnes (1989). Rupture of the 4 February 1976 Guatemalan earthquake, *Bull. Seism. Soc. Am.* **79**, 670–689.

## Appendix

We calculate the  $\beta$ -statistic as described in Matthews and Reasenberg (1988). This quantity compares the number of earthquakes observed after the mainshock,  $n_a$ , in time period,  $t_a$ , and the number expected,  $E(n_a)$ , if earthquake occurrence were to continue at the rate before the mainshock.  $E(n_a) = r \cdot t_a$ , where  $r = n_b/t_b$  is the ambient rate of earthquakes estimated from a background period,  $t_b$ , before the mainshock and  $n_b$  is the number of earthquakes in the background period. The difference between  $n_a$  and  $E(n_a)$  is normalized by the variance of  $n_a$ ,  $\text{var}(n_a)$ . For a binomial distribution  $\text{var}(n_a) = Npq$  where  $p = t_a/T$ ,  $q = 1 - p = t_b/T$ ,  $T = t_a + t_b$  and  $N = n_a + n_b$ . Because the observed value of  $n_a$  may be anomalous (e.g., if triggering occurred),  $E(n_a)$  is used in its place, and  $N = n_b(1 + t_a/t_b)$ . Thus, the  $\beta$ -statistic is defined as

$$\beta = \frac{n_a - E(n_a)}{\sqrt{\text{var}(n_a)}} = \frac{n_a - n_b(t_a/t_b)}{\sqrt{n_b t_a / T}} \quad (1)$$

Kilb *et al.* (2000) used a modified version of the  $\beta$ -statistic, which did not assume that the post-mainshock period may be anomalous. In this case  $E(n_a)$  is calculated assuming the ambient rate is  $r = N/T$  and is not substituted for  $n_a$  when calculating  $\text{var}(n_a)$ . However, Kilb *et al.* (2000, 2002) used both approaches and found the difference to be insignificant.

We comment on estimating rate change in regions where there are no earthquakes observed during the background period. This situation does not imply that the ambient rate is zero. Noting that earthquake counts are inherently discrete, the observation  $n_b = 1$  and  $n_b = 2$  implies  $1 < E(n_b) < 1.5$  and  $1.5 < E(n_b) < 2.5$ , respectively. Similarly, the observation  $n_b = 0$  implies  $0 < E(n_b) < 0.5$ ; in these cases we use  $n_b = 0.25$  in equation (1).

U.S. Geological Survey  
Center for Earthquake Research and Information  
3876 Central Ave., Suite 2  
Memphis, Tennessee, 38152-3050  
*gomberg@usgs.gov*  
(J.G.)

Center for Earthquake Research and Information  
University of Memphis  
3876 Central Ave., Suite 1  
Memphis, Tennessee, 38152-3050  
*bodin@ceri.memphis.edu*  
(P.B.)

U.S. Geological Survey, MS 977  
345 Middlefield Rd.  
Menlo Park, California, 94025  
*reasen@usgs.gov*  
(P.A.R.)

Manuscript received 1 March 2002.